The Energy Budget of the Polar Atmosphere in MERRA

RICHARD I. CULLATHER
Earth System Science Interdisciplinary Center, University of Maryland, College Park

MICHAEL G. BOSILOVICH
Global Modeling and Assimilation Office,
NASA Goddard Space Flight Center, Greenbelt, Maryland

Submitted to: *Journal of Climate*

Corresponding author address: Richard Cullather, % NASA/GSFC Code 610.1,
8800 Greenbelt Road, Greenbelt, MD 20771.
E-mail: richard.cullather@nasa.gov

ABSTRACT

Components of the atmospheric energy budget from the Modern Era Retrospective-analysis for Research and Applications (MERRA) are evaluated in polar regions for the period 1979-2005 and compared with previous estimates, in situ observations, and contemporary reanalyses. Closure of the energy budget is reflected by the analysis increments term, which results from virtual enthalpy and latent heating contributions and averages −11 W m^{-2} over the north polar cap and −22 W m^{-2} over the south polar cap. Total energy tendency and energy convergence terms from MERRA agree closely with previous study for northern high latitudes but convergence exceeds previous estimates for the south polar cap by 46 percent. Discrepancies with the Southern Hemisphere transport are largest in autumn and may be related to differences in topography with earlier reanalyses. For the Arctic, differences between MERRA and other sources in TOA and surface radiative fluxes maximize in May. These differences are concurrent with the largest discrepancies between MERRA parameterized and observed surface albedo. For May, in situ observations of the upwelling shortwave flux in the Arctic are 80 W m^{-2} larger than MERRA, while the MERRA downwelling longwave flux is underestimated by 12 W m^{-2} throughout the year. Over grounded ice sheets, the annual mean net surface energy flux in MERRA is erroneously non-zero. Contemporary reanalyses from the Climate Forecast Center (CFSR) and the Interim Re-Analyses of the European Centre for Medium Range Weather Forecasts (ERA-I) are found to have better surface parameterizations, however these collections are also found to have significant discrepancies with observed surface and TOA energy fluxes. Discrepancies among available reanalyses underscore the challenge of reproducing credible estimates of the atmospheric energy budget in polar regions.

1. Introduction

The objective of this study is to examine the performance of the Modern Era Retrospective-analysis for Research and Applications (MERRA) in representing the high latitude atmospheric energy budget. MERRA was recently released by NASA's Global Modeling and Assimilation Office (GMAO). This effort, as well as a companion paper examining the atmospheric moisture budget (Cullather and Bosilovich, 2010), represent an initial examination of this reanalysis in the polar regions.

A quantitative knowledge of the flow, storage, and conversion of energy within the climate system has evolved with time as a result of contributions made by improvements in the observing system and by numerical atmospheric reanalyses (e.g., Fasullo and Trenberth, 2008). In the polar regions the energy budget and its variability are frequently used as a diagnostic for understanding rapidly changing conditions including glacial mass balance and perennial sea ice reduction (e.g., Porter et al., 2010). As noted in Cullather and Bosilovich (2010), numerical reanalyses are widely used in polar research for evaluating polar processes, as boundary conditions for limited area atmosphere and ocean–sea ice models, and as a first-order validation for climate models. However reanalyses inevitably contain inaccuracies resulting from limitations in the observing system, inconsistencies between differing observations, and incomplete knowledge of the physical processes that are represented in the assimilating weather forecast model. In particular, surface albedo characteristics over polar oceans and high latitude cloud properties are both associated with important but complex energy feedback mechanisms that have historically been poorly simulated (Randall et al., 1998). An initial evaluation of the high latitude energy budget in a reanalysis record is therefore a constructive activity.

Some questions of interest pertaining to this study are as follows.

- What are the spatial and temporal patterns of energy budget components in MERRA, and how do they compare with previous studies and contemporary reanalyses?
- How do MERRA surface fluxes compare with in situ field studies?
- What is the nature of adjustment terms in the energy budget?

Section 2 provides an overview of the MERRA data set and method. An evaluation of the atmospheric energy balance in polar regions is given in section 3. A discussion of these comparisons is then given in section 4.

2. MERRA description and method

Specification of the MERRA system is given in Cullather and Bosilovich (2010) and Rienecker et al. (2010). MERRA utilizes the incremental analysis update assimilation method (IAU; Bloom et al., 1996). In this method, a tendency is computed from the difference between an initial 6-hourly analysis field and the background forecast model state. The forecast model is then run a second time over the six-hour interval using this tendency as an additional forcing term. The resulting MERRA product is then composed of dynamically-consistent one-hourly fields that are incrementally corrected to observation every six hours. Thus atmospheric budgets– as they are constructed in the GEOS-5 AGCM– and their analysis increments are maintained within MERRA to the accuracy limited by round-off and data compression errors.

Following a form similar to Trenberth (1997), the MERRA total energy equation integrated over the atmospheric column may be written as

$$\frac{\partial A_E}{\partial t} + \nabla \cdot \tilde{\mathbf{F}}_A = R_{top} + F_{sfc} + L_v \frac{\partial W_v}{\partial t}\bigg|_{CHM} + \left[L_v \frac{\partial W_v}{\partial t} - L_f \frac{\partial W_i}{\partial t} \right]_{FIL} + ANA_{(E)} - Q_{NUM}, \qquad (1)$$

where A_E is total energy in the atmospheric column, $\tilde{\mathbf{F}}_A$ is the horizontal transport of total atmospheric energy, R_{top} is the downward net radiative flux at the top of the atmosphere (TOA), F_{sfc} is the upwelling net surface flux, L_v is the latent heat of vaporization, L_f is the latent heat of fusion, W_v is column-integrated water vapor (precipitable water), W_i is column-integrated cloud ice condensate, $ANA_{(E)}$ is the sum of analysis increments from the IAU method, and Q_{NUM} is the sum of spurious numerical adjustments. The time rate of change in total atmospheric energy storage A_E is expressed as

$$\frac{\partial A_E}{\partial t} = L_v \frac{\partial W_v}{\partial t} - L_f \frac{\partial W_i}{\partial t} + \frac{\partial}{\partial t}\left\{ \int_{p_{top}}^{p_{sfc}} (c_P T_v + \Phi_S + k) \frac{dp}{g} \right\} \quad , \tag{2}$$

where p_{sfc} is surface pressure, p_{top} is the fixed pressure at the top model level which is 0.01 hPa, c_P is the specific heat of the atmosphere at constant pressure, T_v is virtual temperature, Φ_S is surface geopotential, $k = \frac{1}{2}\left|\tilde{\mathbf{V}}\right|^2$ is kinetic energy, and g is the gravity constant. The product $c_p T_v$ is referred to as virtual enthalpy. The divergence term may be expanded as follows:

$$\nabla \cdot \tilde{\mathbf{F}}_A = \nabla \cdot \int_{p_{top}}^{p_{sfc}} (L_v q_v - L_f q_i) \tilde{\mathbf{V}} \frac{dp}{g} + \nabla \cdot \int_{p_{top}}^{p_{sfc}} c_P T_v \cdot \tilde{\mathbf{V}} \frac{dp}{g} + \nabla \cdot \int_{p_{top}}^{p_{sfc}} \Phi \cdot \tilde{\mathbf{V}} \frac{dp}{g} + \nabla \cdot \int_{p_{top}}^{p_{sfc}} k \cdot \tilde{\mathbf{V}} \frac{dp}{g} \quad , \tag{3}$$

where Φ is geopotential within the atmospheric column. The net upward surface flux is given as

$$F_{sfc} = Q_H + Q_E + L_f P_s - R_{sfc} \quad , \tag{4}$$

where Q_H and Q_E are the upwelling surface turbulent sensible and latent heat fluxes, the product $L_f P_s$ is latent heating resulting from solid precipitation, and R_{sfc} is the net downward radiative flux at the surface. The tendency imposed by the analysis increments $ANA_{(E)}$ represents the summation of latent heat, virtual enthalpy, kinetic, and geopotential energy term contributions. Finally, Q_{NUM} in (1) denotes the contribution of spurious residuals resulting from inertial terms,

87 the discretization of the thermodynamic equation, coordinate remapping during model
88 integration, and time-truncation errors. The relation between MERRA variables and equation
89 notation is given in the appendix.
90 The approach of this study is to evaluate MERRA values against prior studies for large-
91 scale areal averages of the terms in (1-4) over fixed polar regions as shown in Fig. 1, with a
92 particular focus on the polar caps. Studies for comparison include Nakamura and Oort (1988),
93 Genthon and Krinner (1998), Serreze et al. (2007), and Porter et al. (2010). Nakamura and Oort
94 (1988) produced budget estimates for both polar caps using the ocean flux values of Levitus
95 (1984), composite satellite data from the period 1966-1977, and atmospheric circulation statistics
96 from Oort (1983) which are largely based on the upper air station network. Nakamura and Oort
97 (1988) found the observational network insufficient for computing atmospheric energy transport
98 into the south polar cap and instead produced output from the NOAA Geophysical Fluid
99 Dynamics Laboratory GCM. Genthon and Krinner (1998) used the 15-year re-analysis of the
100 European Centre for Medium-Range Weather Forecasts (ECMWF) (ERA-15; Gibson et al.,
101 1997) for the period 1979-1993 to evaluate the south polar cap. Serreze et al. (2007) examined
102 the north polar cap and Arctic Ocean domains using the more recent 40-year re-analysis of
103 ECMWF (ERA-40; Uppala et al., 2005) and the National Centers for Environmental
104 Prediction/National Center for Atmospheric Research Reanalyses (NCEP/NCAR; Kalnay et al.,
105 1996) for the period 1979-2001. Serreze et al. (2007) also examined TOA radiative fluxes from
106 the Earth Radiation Budget Experiment for the study period February 1985 to April 1989
107 (ERBE; Barkstrom, 1984). Porter et al. (2010) similarly examined the north polar cap energy
108 budget for the period November 2000 to October 2005 using the 25-year Japanese Re-Analysis
109 (JRA-25; Onogi et al., 2007), and satellite data from the Clouds and the Earth's Radiant Energy

System (CERES; Wielicki et al., 1996) product. In support of budget comparisons with these previous studies, the evaluation of near-surface state variables against in situ station observations is also instructive.

Corresponding values for surface and TOA energy fluxes are also tabulated for two contemporary reanalyses for comparison: the ECMWF Interim product (ERA-I; Simmons et al., 2007) and the NCEP Climate Forecast System Reanalysis (CFSR; Saha et al., 2010). The ERA-I was produced at T-255 spectral resolution, which is similar to the grid resolution of MERRA. Energy flux fields are produced from 12-hour forecasts initialized by 4D-Var assimilation. Monthly fields of the ERA-I were obtained for the years 1989-2005 at a reduced resolution of 1.5° × 1.5°. The CFSR utilize a coupled atmosphere-ocean model for the initial guess field and an interactive sea ice model and was produced at T-382 spectral resolution. Model variables are produced from 6-hour forecasts. Energy flux fields from the CFSR were obtained at full spatial resolution.

Evidence of an evolving climate system in polar regions– particularly for the Arctic (e.g., Porter et al., 2010)– motivate an exclusion of the most recent years in the available MERRA time series for an averaging period. The results presented here are for the years 1979-2005.

3. Atmospheric energy budget

a. Analysis increments

Terms of the atmospheric energy budget averaged over the period 1979-2005 from MERRA are shown in Table 1 for the polar regions defined in Fig. 1. The far right column indicates budget adjustment quantities. As noted earlier, artificial moisture filling and chemistry parameterization terms of the energy budget from equation (1) have essentially zero magnitude.

133 Not shown, the spatial pattern of the spurious residual Q_{NUM} is characterized by alternating
134 positive and negative values in regions of steep topography. Averages taken over limited areas
135 may produce aliasing of these oscillating values. For example, Q_{NUM} averages 1.5 W m^{-2} over
136 the Greenland Ice Sheet. But in general, $ANA_{(E)}$ is the largest adjustment quantity of interest in
137 the atmospheric energy budget, and its spatial patterns are shown in Fig. 2. Here, positive values
138 indicate an energy surplus in the balance equation while negatives indicate a deficit. The
139 magnitude is a measure of closure obtainable by physical terms. The spatial patterns shown in
140 Fig. 2 are complex, vary with time, and are typically dissimilar to the patterns of the analysis
141 increments for the atmospheric moisture budget shown by Cullather and Bosilovich (2010).
142 As noted previously, analysis increments for the energy budget are the summation of
143 contributions from latent heat, virtual enthalpy, kinetic, and geopotential energy terms. Of these
144 four, the contribution to $ANA_{(E)}$ from virtual enthalpy is large for monthly and annual averages in
145 both polar cap regions, while analysis increments from latent heating are also significant for the
146 north polar cap. For the Northern Hemisphere polar region, negative values for $ANA_{(E)}$ are found
147 over the Arctic Ocean, while positive values are present over surrounding lower latitudes. Mean
148 annual amounts less than −40 W m^{-2} are present in the vicinity of the North Pole with smaller
149 magnitudes over Greenland and marginal seas. Seasonally, these magnitudes are larger in
150 summer than in winter, however the values do not approach the local imbalances of greater than
151 100 W m^{-2} that are shown for the ERA-40 in Serreze et al. (2007). For the average over the north
152 polar cap, $ANA_{(E)}$ ranges from −4 W m^{-2} in February to −17 W m^{-2} in June.
153 In Cullather and Bosilovich (2010), MERRA analysis increments for the atmospheric
154 moisture budget were shown to be characterized by closed contours denoting upper air stations in
155 coastal Greenland and Antarctica. Although signatures of upper air station locations are not as

evident in the $ANA_{(E)}$ field as in the analysis increments field for the atmospheric moisture budget, a dipole is apparent in Fig. 2a in the vicinity of Hudson Strait with centers near Kuujjuaq (58°N, 68°W) and Cape Dorset (64°N, 77°W). Averaged over the north polar cap and the period 1979-2005, $ANA_{(E)}$ is −11 W m^{-2}. The temporal variability of $ANA_{(E)}$ in the Arctic also differs markedly from the analysis increments field of the atmospheric moisture budget presented in Cullather and Bosilovich (2010). Changes in the high latitude atmospheric moisture budget analysis increments were largely found to be associated with the introduction of data from the Advanced Microwave Sounding Unit (AMSU) in November 1998, which has a global impact on MERRA (Bosilovich et al., 2010). In contrast, the $ANA_{(E)}$ time series for the north polar cap indicates changes which are not concurrent with satellite observing system changes. The magnitude of energy budget analysis increments for the north polar cap averages less than 10 W m^{-2} for the period 1979-1991, approximately 18 W m^{-2} over the period 1992-1997, and 9 W m^{-2} thereafter. These shifts may be due to changes in the surface observing system or in atmospheric conditions.

In the Southern Hemisphere, the MERRA energy budget analysis increments term– as shown in Fig. 2b– has a larger magnitude than for the north polar cap, with amounts of greater than (−)80 W m^{-2} over Victoria Land and regions of northern Queen Maud Land in East Antarctica. Over the south polar cap, $ANA_{(E)}$ ranges from −27 W m^{-2} in February to −20 W m^{-2} in August and September. The annual average of $ANA_{(E)}$ is comparatively smaller over the lower latitudes of the Southern Ocean as seen in Fig. 2b. There is a considerable annual cycle for the Southern Ocean domain ranging from −40 W m^{-2} in January and February to −9 W m^{-2} in June. The year to year time series for the south polar cap is highly variable and ranges from −37 W m^{-2} in 1983 to −9 W m^{-2} in 1998. The analysis increments time series for the south polar

179 cap energy budget is uncorrelated with that of the north polar cap, and its relation to changes in
180 the observing system is also not readily apparent. But over the data-sparse Southern Ocean
181 domain there is a discontinuity in the $ANA_{(E)}$ time series in 1998 that is likely associated with the
182 introduction of AMSU. Southern Ocean analysis increments average −21.8 W m^{-2} prior to 1998,
183 and −26.7 W m^{-2} thereafter.
184
185 *b. Total atmospheric energy tendency*
186 In both the north and south polar caps, the MERRA total energy tendency is near zero
187 for annual averages and is small for months of solstice, as shown in Table 1. But there is an
188 oscillatory annual cycle for the tendency terms as seen in Fig. 3. For the north polar cap, the
189 tendency term reaches a maximum of 26 W m^{-2} in April and a minimum of −26 W m^{-2} in
190 September. This annual cycle agrees very closely with values from other reanalyses as reported
191 by Porter et al. (2010), Serreze et al. (2007), and from the observational study of Nakamura and
192 Oort (1988). The RMS difference of monthly means with MERRA is only 4 W m^{-2} for both
193 NCER/NCAR and JRA-25 as reported by Porter et al. (2010), less than 1 W m^{-2} for the ERA-40
194 as reported by Serreze et al. (2007), but 10 W m^{-2} for Nakamura and Oort (1988). In general the
195 reanalyses are more similar to each other than to the earlier Nakamura and Oort time series.
196 For the south polar cap, the total energy tendency in MERRA ranges from a minimum of
197 −16 W m^{-2} in April to 30 W m^{-2} in November. As seen in Fig. 3b, the annual cycle is less
198 sinusoidal than in the Northern Hemisphere, with the November peak offsetting an average
199 negative tendency that extends from January through July. The RMS difference with monthly
200 values reported by Nakamura and Oort (1988) as compared to MERRA is 13 W m^{-2}, although
201 each month is within the standard deviation of MERRA for the 1979-2005 period. As seen in

202 equation (4), the MERRA energy tendency incorporates the cloud ice latent heating and kinetic
203 energy terms which are not considered in other studies. For monthly means over the regions
204 examined, however, these terms are negligible.
205
206 *c. Energy convergence and transport*
207 As seen in equation (3), the divergence term is composed of contributions from latent
208 heat, virtual enthalpy, kinetic, and geopotential energy terms. For the north polar cap, the annual
209 cycle of energy convergence from MERRA consists of values greater than 100 W m^{-2} during
210 winter months September through March and a minimum of 72 W m^{-2} in May, as seen in
211 Fig. 3a. Porter et al. (2010) present annual cycles of energy convergence computed as a residual
212 using several combinations of reanalyses and radiative flux data sets for the period 2000-2005,
213 while Serreze et al. (2007) present ERA-40 and NCEP/NCAR reanalysis average monthly values
214 for the period 1979-2001. While there is agreement in larger energy convergence in winter, there
215 is considerable variability among the data sets on the months of the minimum and maximum
216 value, with May providing a spread of 40 W m^{-2} among the various methods. MERRA values
217 concurrent with these previous studies are found within this large range.
218 Figure 4a indicates that the average poleward energy transport across 70°N is zonally
219 asymmetric and is focused at preferred longitudes which are associated with the mean longwave
220 circulation patterns in the middle troposphere (Serreze et al., 2007). In comparison to energy
221 transports across 70°N from ERA-40 as reported by Serreze et al. (2007), MERRA transports
222 shown in Fig. 4a are comparable but with some differences. First, the poleward (positive) flux
223 centered near 315°E (45°W) has a smaller zonal extent than is shown in Serreze et al. (2007).
224 This may be due to the higher spatial resolution of MERRA and the role of the Greenland Ice

225 Sheet topography in defining the mid-tropospheric trough pattern over eastern North America.
226 Second, the wintertime poleward transport near 150°E is shown in MERRA to be greater than
227 $20 \cdot 10^9$ W m^{-1}. This is stronger by one contour level ($5 \cdot 10^9$ W m^{-1}) than that shown by
228 Serreze et al. for ERA-40. But in general the average meridional transport patterns of MERRA
229 and ERA-40 are remarkably similar.

230 In the Southern Hemisphere, prior studies on atmospheric energy convergence are not as
231 recent. However comparisons to MERRA may be made using Nakamura and Oort (1988) and
232 Genthon and Krinner (1998). Using GCM output, Nakamura and Oort (1988) estimated a mean
233 annual energy convergence across 70°S of 95 W m^{-2}, which is 23 W m^{-2} less than shown for
234 MERRA in Table 1. As seen in Fig. 3b, the annual cycle in MERRA contains a broad maximum
235 over winter months and a short period of minimum of values less than 100 W m^{-2} in December,
236 January, and February. In contrast Nakamura and Oort (1988) indicate lower amounts in the
237 autumn, and their annual cycle is generally more sinusoidal. Nakamura and Oort (1988) and
238 MERRA monthly energy convergence values are comparable over the months June to October
239 but MERRA is larger by 45 W m^{-2} in January. More recently, Genthon and Krinner (1998)
240 produced seasonal averages and zonal distributions of energy transport using ERA-15 for the
241 period 1979-1993. The annual atmospheric energy convergence derived from ERA-15 of
242 81 W m^{-2} is considerably smaller than corresponding values of either MERRA or Nakamura and
243 Oort (1988). Seasonally, the largest differences between MERRA and Genthon and
244 Krinner (1998) ERA-15 values are in autumn. Energy convergence for the south polar cap for
245 March-April-May averages 134 W m^{-2} in MERRA, while Genthon and Krinner (1998) reported
246 79 W m^{-2}. The spatial distribution of energy transports along the 70°S parallel is strongly
247 dependent on the meandering coastline, such that spatial resolution and topography are

248 significant. Thus the differences between MERRA and ERA-15, though large, may partially
249 result from differing model grids. Additionally, ERA-15 was known to employ a defective
250 orography over the ice sheet (Uppala et al., 2005). A visual inspection of Genthon and Krinner
251 (1998) results indicates that the ERA-15 mean annual poleward transport is less than MERRA
252 near 30°E, an intersection point between the 70°S parallel and the East Antarctic coastal
253 escarpment. For this location, Genthon and Krinner (1998) plot amounts of between 2 and
254 $3 \cdot 10^9$ W m^{-1} while MERRA values are greater than $5 \cdot 10^9$ W m^{-1}. Additionally Genthon and
255 Krinner (1998) indicate an annual mean equatorward energy transport in the Ross Sea, while
256 MERRA indicates an average poleward flux. MERRA and ERA-15 share some general
257 characteristics of the meridional energy transport including a directional change with season in
258 the South Pacific region between 180°E and 270°E from poleward during winter months to
259 equatorward in summer , as shown in Fig. 4b. The figure also shows an opposing seasonal
260 reversal between 270°E and 300°E in MERRA, and this is also reflected in Genthon and Krinner
261 (1998).
262
263 *d. TOA radiative fluxes*
264 For the north polar cap, MERRA TOA radiative fluxes are compared to ERBE (Serreze
265 et al., 2007) and CERES (Porter et al., 2010). With the exception of midsummer months, the
266 Arctic TOA radiative flux in MERRA is mainly directed upwards ($R_{top} < 0$), with an annual
267 average shown in Table 1 of −110 W m^{-2}. Annual estimates from ERBE and CERES are within
268 the standard deviation of this value. On the monthly time scale, the largest differences are for the
269 month of May, where the MERRA 1979-2005 value of −23 W m^{-2} compares with −53 W m^{-2} in
270 ERBE (Serreze et al., 2007) and −37 W m^{-2} in CERES (Porter et al., 2010). Using MERRA

averages concurrent with these satellite records, MERRA is less than satellite estimates for May by 29 W m^{-2} as compared to ERBE and by 12 W m^{-2} as compared to CERES. In July, CERES indicates a net downwards TOA flux of 21 W m^{-2} compared to a 1 W m^{-2} upwards flux in MERRA, while ERBE and MERRA concurrent July values are equal. For other months, the differences are small.

Table 2 also presents R_{top} values for MERRA in comparison to contemporary reanalyses of the ERA-I and CFSR for the period 1989-2005. As seen in Table 2 for the north polar cap, the MERRA annual net TOA radiative flux is greater than for the other two reanalyses by 4 W m^{-2}. Again, the largest differences are for the spring time period. For the month of May, R_{top} for the ERA-I averages -34 W m^{-2} while the CFSR value is -36 W m^{-2}, and MERRA again averages -23 W m^{-2} for 1989-2005. Most of this difference is associated with the upwelling shortwave flux. For the month of May, the MERRA TOA upwelling shortwave flux is less than CFSR and ERA-I by 15 W m^{-2} and 18 W m^{-2}, respectively. It is noted that CFSR incorporates an 11-year solar cycle while MERRA and ERA-I use climatological solar forcing, and that ERA-I uses a larger solar constant value than MERRA. For the north polar cap, differences in incoming solar radiation between MERRA and CFSR are as large as ±3 W m^{-2} for a given month, but average less than 1 W m^{-2}. Differences between ERA-I and MERRA are as large as 9 W m^{-2} for a given month, and average 3 W m^{-2}.

For the south polar cap, the TOA net radiative flux remains negative throughout the year. Comparisons to both ERBE data and the values from Nakamura and Oort (1988) indicate that the annual net TOA radiative flux magnitude in MERRA is too large, and that the discrepancy is largest during winter months. The 1979-2005 average net flux as shown in Table 1 for MERRA is -101 W m^{-2}. This compares with -90 W m^{-2} from the historical satellite data used in

294 Nakamura and Oort (1988), and −95 W m^{-2} from ERBE for the period February 1985 to April
295 1989 (Briegleb and Bromwich, 1998). The 1979-2005 annual average for R_{top} is by chance equal
296 to the 1985-1989 time period for MERRA. In the annual cycle, the differences with satellite
297 observations are associated with the winter season. For the months of June, July, and August, the
298 average flux from Nakamura and Oort (1988) is −131 W m^{-2}, and from ERBE, −134 W m^{-2}.
299 For MERRA, the corresponding value is −142 W m^{-2} for both 1979-2005 and 1985-1989 time
300 periods. In these winter months, the difference between MERRA and satellite values is almost
301 entirely composed of the outgoing longwave component.
302 Values for the south polar cap from ERA-I and CFSR reanalyses tend to agree more
303 closely with MERRA than with values from satellite data sets. For the 1989-2005 period, the net
304 TOA radiative flux shown in Table 2 averages -101 W m^{-2} for MERRA, -109 W m^{-2} for CFSR,
305 and -102 W m^{-2} for ERA-I. In the annual cycle, the MERRA upwelling longwave flux is less
306 than the other two reanalyses by 3 W m^{-2} in spring and up to 7 W m^{-2} in autumn. The CFSR
307 upwelling shortwave flux is greater than the other two reanalyses by more than 10 W m^{-2} in
308 December and January, and the ERA-I solar constant difference with the other two reanalyses
309 accounts for 3 W m^{-2} on the annual average.
310 The time series of MERRA TOA radiative fluxes indicate potentially spurious trends in
311 both polar regions. Over north and south polar caps, year to year variability in R_{top} resembles that
312 of the energy budget analysis increments. For the north polar cap, a maximum for R_{top} is reached
313 in 1993 with −107 W m^{-2}, with values as low as −112 W m^{-2} occurring in 1981 and 2005.
314 MERRA TOA fluxes for the south polar cap have an irregular time series with a range between
315 minimum and maximum values of 4 W m^{-2}. Over the Southern Ocean domain, a sharp change is
316 noted after 1998. This is likely due to the introduction of AMSU data to the observing system as

noted earlier. Annual average values prior to 1998 are consistent with an average of −81 W m^{-2}. For the period 1999-2005 the MERRA average for the Southern Ocean is −86 W m^{-2}.

e. Surface fluxes

Figure 5 shows the annual average surface net heat flux from MERRA for both polar regions. In the Northern Hemisphere, small negative values of between 0 and −5 W m^{-2} are found in a uniform field over nonglaciated land surfaces, which is consistent with subsurface warming in recent years (Serreze et al., 2007). Over the central Arctic Ocean, MERRA net surface flux values are positive as expected but are exceptionally large. Values greater than 15 W m^{-2} are found in the central Arctic, and greater than 20 W m^{-2} in the approaches to the North Atlantic. These annual values are extraordinary and likely not realistic. A comparison of the averaged annual time series of monthly values with previous studies indicates largest discrepancies occurring in summer months. The July 1979-2005 net surface flux for MERRA is −68 W m^{-2} for the north polar cap as shown in Table 1. This compares with −85 W m^{-2} for ERA-40 (Serreze et al., 2007) and −86 W m^{-2} for JRA-25 (Porter et al., 2010). Similar differences are found between MERRA and contemporary reanalyses as shown in Table 2. For the concurrent 1989-2005 averaging period, the July net surface flux for the north polar cap is −87 W m^{-2} for the CFSR and −78 W m^{-2} for ERA-I.

Discrepancies in the surface flux fields are evaluated using observations from the Surface Heat Budget of the Arctic ice camp field study in the Beaufort Sea in October 1997 to October 1998 (SHEBA; Uttal et al., 2002). MERRA surface flux values are compared with a compilation of observed SHEBA radiative and turbulent flux measurements by Duynkerke and de Roode (2001). Comparisons are made using the nearest MERRA grid point to the reported hourly drift

340 camp position. For this data source, SHEBA latent heat flux observations were limited and are
341 not considered. Using the remaining energy budget components, a net flux comparison indicates
342 a positive (upward) bias in MERRA of 18 W m^{-2} for the months October to April, −1 W m^{-2} for
343 May, and small positive biases for the following summer months.
344 There are three fundamental results of the comparison. As shown in Fig. 6, substantial
345 differences in the upwelling shortwave radiative flux result from an overly simplistic
346 representation of sea ice properties. Sea ice albedo is set to a fixed value of 0.60 for MERRA.
347 The surface observed using SHEBA tower measurements has a much higher albedo in
348 springtime, with monthly averages of 0.83 in March, April, and May, and 0.74 in June. Apart
349 from the tower flux measurements, a line of surface albedo observations made during SHEBA
350 provide a range of values that are dependent on the surface ice conditions. The average of these
351 surface observations is shown in Fig. 6 for June to September 1998. Albedos from tower
352 measurements in May 1998 are consistent with area-averaged surface and aircraft observations.
353 For example, Curry et al. (2001) note that albedo for April and May at the SHEBA site averaged
354 0.84, that the melt season lasted from late May to mid August, and that winter-spring albedo
355 values were again reached in late September. This difference with observed albedo contributes to
356 an underestimate in the upwelling shortwave flux in MERRA of 55 W m^{-2} in April, 80 W m^{-2} in
357 May, and 56 W m^{-2} in June. In late summer, the observed surface albedo is degraded by melting
358 and becomes comparable to the MERRA value. In late autumn, freezing and the introduction of
359 solid precipitation again produces surface albedo differences between MERRA and observation,
360 however the incoming solar flux is reduced and the impact on the upwelling shortwave is less
361 consequential. The difference with observation in the upwelling shortwave radiative flux for
362 May is the largest of any monthly budget component.

363 The second result is a response in other MERRA surface energy budget terms in May to
364 the albedo bias. Surface temperatures over ice in MERRA are determined via energy balance,
365 and the underestimate of the surface albedo results in a perceived increased absorption of solar
366 energy and a surface warming. This likely results in the springtime MERRA sensible heat flux
367 bias, which is found to be 16 W m^{-2} in May. Other than the April, May, and June period, the
368 MERRA sensible heat flux difference with SHEBA observations is only 2 W m^{-2}. An intriguing
369 finding is a springtime negative bias with SHEBA observations in the downwelling shortwave
370 radiative flux. The MERRA downwelling shortwave is underestimated by 36 W m^{-2} in April,
371 37 W m^{-2} in May and 25 W m^{-2} in June. In other months this difference is about 1 W m^{-2}. This
372 bias is likely associated with general deficiencies in the representation of cloud properties. From
373 the seasonal timing of the bias, however, it is speculated that a portion of the amount is due to a
374 redistribution of cloudiness in the atmospheric column resulting from anomalous surface
375 warming. The large May bias in upwelling shortwave radiation is then compensated for by biases
376 in other fluxes to produce the surface net energy flux bias of -1 W m^{-2}.
377 Shown in Fig. 7 is the time series of hourly near-surface air temperature in comparison to
378 the observed time series from SHEBA for the period 1 February to 30 June,1998. A temperature
379 bias in spring is readily apparent, with a difference of greater than 3.5°C in April and May before
380 the freezing value is reached in early June. In particular, the period 19 April to 10 May shows an
381 average bias of 6.1°C in MERRA. For daily averages, however, there is a good correlation
382 between MERRA and observation for the period shown ($r = 0.95$). It may be seen in the time
383 series of hourly values shown Fig. 7 that the diurnal cycle in MERRA temperature has an
384 amplitude between 2 and 10°C, which begins abruptly on 28 March and continues unabated until
385 the freezing point is reached in June. The observed SHEBA diurnal cycle has a similar

386 amplitude, however the cycle is not as regular as in MERRA and there are periods of
387 considerable interruption, perhaps due to synoptic variability. These differences are suggestive of
388 difficulties in MERRA boundary layer parameterizations. Springtime air temperature biases are
389 found at Arctic station locations as well. For example, a comparison with Sachs Harbor (72°N,
390 125°W) over the period 1979-2005 indicates an average of 4.9°C difference for April but only
391 1.9°C for the months August through March. A comparison with Barrow (71°N, 157°W)
392 similarly indicates an average bias in MERRA of 3.6°C for the spring months of March, April,
393 and May and 0.9°C for other months. But as shown in Fig. 8, MERRA performs well in a
394 comparison of monthly anomalies. The correlation between temperature anomalies at Barrow
395 and Jan Mayan (71°N, 9°W) is 0.99 for both stations. The time series shown in Fig. 8 contain
396 observations that cover the entire time period. Other stations in the Arctic with shorter and/or
397 interrupted records compare similarly well.

398 The third result from the comparison with SHEBA is a negative bias in the downwelling
399 longwave radiative flux throughout the year of 12 W m^{-2}. This quantity leads to the overall
400 positive bias in the net surface flux for summer, autumn, and winter months. As with the
401 springtime downwelling shortwave radiative flux bias, an inadequate representation of cloud
402 properties is implied. To evaluate this further, comparisons were made between MERRA and
403 SHEBA hourly microwave radiometer retrievals over the period 5 December 1997 to
404 9 September 1998. More than 5000 observations were made over the period. Retrievals of
405 precipitable water compare remarkably well to MERRA values as seen in Fig. 9a, although
406 differences are apparent for small quantities in winter. For monthly intervals, the correlation
407 between MERRA and the hourly microwave radiometer precipitable water retrievals ranges from
408 $r = 0.87$ in December 1997 to $r = 0.96$ in May 1998. A consistent bias of 0.6 mm in monthly

409 averages is found, which amounts to 31 percent of the observed average for January but only
410 3 percent for July. In contrast, the comparison to retrieved liquid water content shown in Fig. 9b
411 is less favorable. Cloud liquid water from the SHEBA microwave radiometer ranges from an
412 average of 0.017 mm in January 1997 to 0.106 mm in August 1998. Typical MERRA values are
413 about 45 percent of the microwave radiometer amounts. Although large discrepancies have been
414 noted between the SHEBA microwave radiometer values for liquid water path and simultaneous
415 aircraft measurements (Lin et al., 2001), the differences between MERRA and SHEBA values
416 exceed 50 percent. Additionally, the correlations of hourly liquid water path values with
417 MERRA over monthly time intervals are low and range from $r = 0.14$ in April 1998 to $r = 0.55$ in
418 January 1998. The presence or absence of cloud liquid water significantly alters the downwelling
419 longwave radiative flux. An underestimate of cloud liquid water in MERRA is qualitatively
420 consistent with differences in the surface net flux with observation.

421 Comparisons with MERRA for the Arctic are also conducted using the CFSR and ERA-I
422 reanalyses. Using monthly values co-located with the SHEBA ice drift camp, it is noted that
423 surface albedo varies seasonally and interannually in both CFSR and ERA-I. In agreement with
424 the SHEBA time series, both CFSR and ERA-I have albedos greater than 0.8 for April 1998, and
425 values decrease with the onset of the summer melt season. This decrease occurs more rapidly in
426 both CFSR and ERA-I than for tower observations, but is within the lower range given by
427 SHEBA line albedo measurements. The June 1998 albedo is 0.59 for MERRA, 0.65 for CFSR,
428 0.69 for ERA-I, 0.74 for the SHEBA tower observation, and 0.62 for the line observation. All
429 three reanalyses underestimate the downwelling longwave radiative flux over winter months in
430 comparison to SHEBA. For the period October 1997 to May 1998, this flux is underestimated by
431 5 W m^{-2} in ERA-I and 18 W m^{-2} in CFSR. Finally, the November 1997 to March 1998 average

sensible heat flux observed at SHEBA is less than 1 W m^{-2}. This compares with 3 W m^{-2} in MERRA, −7 W m^{-2} in ERA-I, and −21 W m^{-2} in CFSR.

Turning to the Southern Hemisphere, the annual average net surface heat flux for the south polar cap is shown in Fig. 5b. Of immediate concern is the anomalous non-zero field over Antarctica, which is shared by the major ice sheets in both polar regions. Over grounded ice, the MERRA subsurface energy flux is determined in the GEOS-5 model by the prognostic temperature for a 7 cm (water-equivalent) surface ice layer and a "deep" layer temperature at 2 m depth that is fixed at 230°K. Thus, the location of the zero value contour in Fig. 5b exactly matches the annual-average 230°K surface temperature isotherm. Observations from automatic weather stations indicate that annual mean subsurface conductive heat fluxes are not significant (e.g., Reijmer and Oerlemans, 2002), and annual surface energy flux patterns in MERRA over Antactica (as well as Greenland) are erroneous.

The pattern in the MERRA annual surface net energy flux in Antarctica is manifest as a complementary distribution of downward (negative) turbulent and upward (positive) radiative fluxes that are not balanced. MERRA annual mean latent heating exceeds 5 W m^{-2} only along the East Antarctic coast in selected locations, and averages less than 1 W m^{-2} for the total grounded ice sheet area. The annual averaged sensible heat flux over the ice sheet is uniformly negative and is approximately contour-parallel with topography, with magnitudes greater than (−)60 W m^{-2} along the East Antarctic coastal escarpment decreasing to less than (−)10 W m^{-2} over the central plateau. The annual mean net radiative flux field in MERRA is spatially more uniform with values ranging from (+)25 to 35 W m^{-2} for East Antarctica, and smaller positive values over West Antarctica. This results in the imbalances in the net surface heat flux as shown. Over the interior plateau, net flux values are as large as +15 W m^{-2} while the net amounts at

455 lower elevations are negative and are less than −30 W m^{-2} over the East Antarctic coastal
456 escarpment. These errors in the net surface flux have relation to near-surface temperature biases.
457 As shown in Fig. 10, there is a considerable wintertime warm bias of 5°C at Amundsen-Scott
458 (90°S), while a summer cold bias of 5°C is found at Scott Base (78°S, 167°E). Visual
459 comparison with satellite-derived surface air temperatures in Comiso (2000) indicates that a
460 summer cold bias extends over the embayment regions.
461 Comparisons of surface energy budget components are made with Antarctic station
462 values compiled by King and Turner (1997). Values compiled by King and Turner (1997) reflect
463 studies of opportunity and do not account for interannual variability. For the sensible heat flux,
464 MERRA averages at Mizuho (71°S, 44°E) of −47 W m^{-2} in July and −19 W m^{-2} in December
465 compare with observational values of −37 and −25 W m^{-2} for July and December, respectively
466 (Ohata et al., 1985). At South Pole, differences in seasonal values of the sensible heat flux are
467 largest in spring and summer. The December-January-February sensible flux average from
468 MERRA is −3 W m^{-2} and −22 W m^{-2} in observation (Carroll, 1982). This contributes to a
469 difference of 9 W m^{-2} in the annual average.
470 Differences between MERRA and available observations are also associated with the net
471 radiative flux. At Halley (76°S, 26°W), the annual average net radiative flux for MERRA of
472 13 W m^{-2} approximates the observational values of 9.8 W m^{-2}, however seasonal differences are
473 as large as 10 W m^{-2} in winter. At South Pole, the annual net radiative flux of 19 W m^{-2} matches
474 the observation of Carroll (1982), however seasonal differences are large. In winter, the net
475 radiative surface cooling of 36 W m^{-2} exceeds the observed value of 21 W m^{-2}. In summer, the
476 MERRA radiative flux value of −7 W m^{-2} differs from the Carroll (1982) value of +18 W m^{-2}.

477 The surface radiative flux differences at South Pole are further examined using the
478 observations of Dutton et al. (1989), who recorded daily mean radiative flux components from
479 April 1986 until February 1988. Over this period, the surface net radiative flux for both MERRA
480 and observation is positive for most of the year but becomes negative in summer months as seen
481 in Fig. 11. Over the 22 month period, the downwelling longwave radiative flux is consistently
482 less than observation by an average 24 W m^{-2}. This difference is apparent in the comparison of
483 daily values in Fig. 11. Large biases are also found in the MERRA net shortwave radiative flux
484 in spring and summer. For the month of January, the net downward shortwave flux is
485 overestimated by 20 W m^{-2} in 1987, and by 23 W m^{-2} in 1988. A minor part of the shortwave
486 bias is associated with the MERRA surface albedo, which is fixed over land ice at 0.775.
487 Observed monthly averages at South Pole indicate an albedo of between 0.80 and 0.89. These
488 differences in the shortwave flux partially cancel the downwelling longwave underestimate in
489 summer. It may be seen from Fig. 11 that some of the day-to-day variability in the downwelling
490 longwave radiative flux is reproduced in MERRA. By subtracting a 30-day running mean from
491 each time series to remove the annual cycle, the two curves have a correlation of 0.70.
492 Table 2 presents a comparison of net surface flux values for the south polar cap. Both the
493 ERA-I and the CFSR correctly depict a near-zero annual net flux field over the Antarctic ice
494 sheet, while regions of opposite sign in MERRA F_{sfc} fortuitously cancel. Monthly values of
495 surface radiative flux components from CFSR and ERA-I are compared to 1986-1988 values
496 from Dutton et al. (1989) for the South Pole. The ERA-I collection begins in 1989, so 1989-2005
497 averages were used. In general, the monthly net surface radiative fluxes of the three reanalyses
498 are more similar to each other than to observation. The net upward radiative flux is
499 overestimated by 18 W m^{-2} for MERRA, 16 W m^{-2} for ERA-I, and 20 W m^{-2} for CFSR. Similar

500 to MERRA, a large part of the ERA-I difference is due to an underestimate of the downwelling
501 longwave component. For the annual average, the ERA-I downwelling longwave flux is
502 underestimated by 15 W m^{-2}. For the CFSR, the upwelling longwave flux is overestimated for
503 winter months March to September by 21 W m^{-2}, and this provides a significant contribution to
504 annual net flux differences. Both ERA-I and CFSR have variable surface albedos at South Pole,
505 however the ERA-I value approximates the MERRA fixed value, while the CFSR value averages
506 0.84 during summer months.
507 The spatial patterns of Fig. 5b are of interest over the Southern Ocean. In the annual
508 mean, MERRA indicates a net loss of energy from the ocean to the atmosphere south of 60°S
509 which increases in magnitude near the continent. Farther north there is a marked asymmetry
510 within the 50°S-60°S zone, with net energy loss from the ocean to the atmosphere in the Pacific
511 sector and energy gains elsewhere. Embedded within the Pacific sector are two regions of net
512 energy gain from the atmosphere to the ocean which correspond to meanderings of the Antarctic
513 Polar Front– as it crosses the Southeast Indian Ridge near 145°E, and the Pacific-Antarctic Ridge
514 near 145°W (e.g., Moore et al., 1999). Josey (2009) noted the zonal asymmetry in the net surface
515 heat flux in NCEP and ECMWF reanalyses but found that coupled models produce a more
516 zonally uniform field. Josey (2009) concluded that the sign of annual mean surface heat
517 exchange over much of the region is not known. The net surface flux from ERA-I and CFSR
518 reanalyses in Southern high latitudes differ with MERRA. The coastal zone of heat loss from the
519 ocean to the atmosphere in both the ERA-I and CFSR is more closely confined near the continent
520 than in MERRA. Similar to MERRA, the ERA-I indicates an annual mean net positive energy
521 flux from the ocean to the atmosphere in the Pacific Ocean sector of the 50°S-60°S zone, while

522 the CFSR indicates negative values between 0 and -15 W m^{-2} that are smaller in magnitude than
523 for the rest of the zone.

524 The annual cycle of the net surface flux for the Southern Ocean is shown in Fig. 3c.
525 Using ECMWF operational analyses overlapping the period of the ERBE study, Okada and
526 Yamanouchi (2002) examined the atmospheric energy budget for the region bounded by 60°S
527 and 70°S. Okada and Yamanouchi estimated the surface energy budget as the residual using
528 TOA ERBE radiation and analyses divergence terms. A seasonal asymmetry in the net surface
529 flux was highlighted, which was found to abruptly peak in May with a maximum value of
530 116 W m^{-2}. Okada and Yamanouchi (2002) attributed this asymmetry to the latent heat release
531 resulting from sea ice formation. As seen in Fig. 3c, the MERRA surface energy flux over the
532 Southern Ocean sea ice domain is also asymmetric and peaks in May at 98 W m^{-2}, however the
533 maximum is not as striking as was found for the ECMWF analyses. In examining the autumnal
534 surface turbulent fluxes in MERRA, it is found that the total latent heat flux is a maximum for
535 the domain in April with 33 W m^{-2}. The latent heat flux then diminished over ice covered winter
536 months, with a second maxima in November of 28 W m^{-2}. The MERRA sensible heat flux
537 reaches its annual maximum in May of 21 W m^{-2} and generally reflects the shape of surface net
538 flux. The asymmetry in the annual cycle for the MERRA net surface flux as shown in Fig. 3c is
539 principally due to seasonal changes in the sensible heat flux. In reanalyses, sea ice cover is
540 prescribed from observational fields. The latent heat flux arising from ice formation is manifest
541 as the net conductive flux at the atmosphere-ice interface. In this context, MERRA and the
542 results of Okada and Yamanouchi (2002) are broadly consistent.
543

4. Summary and Discussion

MERRA reproduces the basic patterns of energy flow in the polar atmosphere as they are known. As shown in Fig. 3, the polar regions are marked by a convergence of energy from lower latitudes for all months, and a loss of energy at the top of the atmosphere for the most of the year. In the Arctic, reductions in the TOA shortwave radiative flux in autumn produce a negative tendency in the atmospheric column total energy throughout the period August through January, which is moderated by contributions from the net surface flux and increased energy transport from lower latitudes in winter (Serreze et al., 2007). In the Antarctic, this seasonal progression is less sinusoidal, with the net TOA radiative flux remaining negative throughout the year, and an extended winter period in the energy budget components extending from April to September.

Despite reproducing these essential components, MERRA energy budgets for the Arctic and Antarctic contain substantial errors owing to overly simplistic physical parameterizations, including sea ice albedo, the surface heat budget over permanent land ice, and cloud radiative properties. Difficulties in MERRA with sea ice characteristics are not dissimilar from those described in Bretherton et al. (2000) for ECMWF analyses produced during SHEBA, and indeed the discrepancies in surface shortwave radiative fluxes are similar. Spring is a critical period for evaluation of surface flux fields in the Arctic, and differences between MERRA shortwave surface radiative fluxes with observation are most prominent in May. Over the data sparse Southern Ocean, discontinuities in the time series of TOA radiative fluxes coincide with the introduction of AMSU satellite data in November 1998 and are therefore spurious. Elsewhere, interannual variability of the analysis increments term $ANA_{(E)}$ is large but not as easily linked to changes in the observing system. Additional characterization of analysis increments, including

566 their vertical distribution, and MERRA cloud properties are conspicuous points for further
567 evaluation.
568 MERRA nevertheless compares favorably to previous studies of energy budget
569 components produced from state and dynamical variables. These vertical integrals are pre-
570 computed quantities in MERRA, and are not readily available from contemporary reanalyses.
571 Atmospheric energy convergence and the spatial distribution of transport along the 70° parallel
572 compare closely with previous studies in the Northern Hemisphere, while estimates for the south
573 polar cap are qualitatively similar but may also been seen as an update to studies based on earlier
574 analyses. The total atmospheric energy tendency in polar regions also compares favorably to
575 previous studies.
576 Credible estimates of the atmospheric energy budget in polar regions continue to be a
577 significant challenge due to changes in the observing system and complex energy feedback
578 mechanisms that are associated with the high latitudes. Evaluation using both representative
579 point location observations and previous area-averaged estimates such as those used in this study
580 are valuable for providing a straightforward appraisal of new reanalyses. The MERRA system is
581 an important product due to its alternative construction, including a non-spectral background
582 model and its emphasis on NASA satellite products. An important concept used in MERRA is
583 the employment of analysis increments for identifying differences between observations and the
584 background analysis system. Inconsistencies in atmospheric budgets are quantified in the
585 analysis increments, which is one means of measuring uncertainty. ERA-I and CFSR reanalyses
586 are found to utilize seasonal variations in sea ice albedo and have realistic annual mean surface
587 heat fluxes over ice sheets. However these collections are also found to have significant
588 discrepancies with observed surface and TOA energy fluxes. In particular, sensible heat fluxes

589 from CFSR are large in comparison to SHEBA observations, while all three reanalyses
590 overestimate the annual surface net radiative flux at South Pole by 16 to 20 W m^{-2}. These
591 disagreements underscore the challenge of the high latitude energy budget problem.
592 A general criticism of reanalyses is that they are produced with the intent of providing the
593 best representation of conditions for a given time without consideration for the impact of
594 heterogeneous observations on temporal variability (Thorne and Vose, 2010). This intent
595 nevertheless has practical, scientific application. Additionally, reanalyses may be seen as part of
596 a spectrum of products for climate study ranging from heterogeneous observations to model
597 simulations, which include AMIP fields and sparse data reanalyses (e.g., Compo et al., 2006). As
598 part of that continuum, the analysis increments in MERRA provides a quantification of
599 differences between observations and the background system. Changes in the spatial and
600 temporal variability of the analysis increments imply changes to the observing system, which
601 should be carefully treated in evaluating time series. MERRA is a valuable record for examining
602 the polar atmosphere when these cautions are exercised.
603
604 *Acknowledgments.* Data from the Surface Heat Budget of the Arctic Ocean experiment
605 (SHEBA) were obtained from the University of Washington Department of Atmospheric
606 Sciences, Seattle, Washington. Reference Antarctic Data for Environmental Research
607 (READER) is a project of the Scientific Committee on Antarctic Research (SCAR) and were
608 obtained from British Antarctic Survey (BAS), Cambridge, United Kingdom. Arctic station
609 values from the Integrated Surface Database (ISD) and the Integrated Rawinsonde Global
610 Rawinsonde Archive (IGRA) were obtained from the National Climate Data Center, Asheville,
611 North Carolina. The ERA-I collection was obtained from the ECMWF Data Server. The CFSR

collection was obtained from the National Climate Data Center. This study was funded by grants from the NASA Modeling Analysis and Prediction Program (MAP) and the NASA Energy and Water cycle Study (NEWS) to the second author.

APPENDIX

Representation of the Atmospheric Energy Budget Using MERRA Variables

The following MERRA variables are given as follows.

DQVDT_DYN	Vertically integrated water vapor tendency for dynamics	kg m^{-2} s^{-1}
DQVDT_PHY	Vertically integrated water vapor tendency for physics	kg m^{-2} s^{-1}
DQVDT_ANA	Vertically integrated water vapor tendency for analysis	kg m^{-2} s^{-1}
DQIDT_DYN	Vertically integrated ice water tendency for dynamics	kg m^{-2} s^{-1}
DQIDT_PHY	Vertically integrated ice water tendency for physics	kg m^{-2} s^{-1}
DQIDT_ANA	Vertically integrated ice water tendency for analysis	kg m^{-2} s^{-1}
DQVDT_CHM	Vertically integrated water tendency for chemistry	kg m^{-2} s^{-1}
DQVDT_FIL	Artificial "filling" of water vapor	kg m^{-2} s^{-1}
DQIDT_FIL	Artificial "filling" of frozen water	kg m^{-2} s^{-1}
DKDT_DYN	Vertically integrated kinetic energy tendency for dynamics	W m^{-2}
DKDT_PHY	Vertically integrated kinetic energy tendency for physics	W m^{-2}
DKDT_ANA	Vertically integrated kinetic energy tendency for analysis	W m^{-2}
DHDT_DYN	Vertically integrated $c_P \cdot T_v$ tendency for dynamics	W m^{-2}
DHDT_PHY	Vertically integrated $c_P \cdot T_v$ tendency for physics	W m^{-2}
DHDT_ANA	Vertically integrated $c_P \cdot T_v$ tendency for analysis	W m^{-2}
DPDT_DYN	Potential energy tendency for dynamics	W m^{-2}
DPDT_PHY	Potential energy tendency for physics	W m^{-2}
DPDT_ANA	Potential energy tendency for analysis	W m^{-2}
CONVKE	Vertically integrated convergence of kinetic energy	W m^{-2}
CONVCPT	Vertically integrated convergence of virtual enthalpy	W m^{-2}
CONVPHI	Vertically integrated convergence of geopotential	W m^{-2}
SWTNT	TOA outgoing shortwave flux	W m^{-2}
SWGNT	Surface net downward shortwave flux	W m^{-2}
LWTUP	Upward TOA longwave flux	W m^{-2}
LWGNT	Net downward longwave flux at the surface	W m^{-2}
EFLUX	Latent heat flux (positive upward)	W m^{-2}
HFLUX	Sensible heat flux (positive upward)	W m^{-2}
PRECSN	Frozen precipitation at the surface	kg m^{-2} s^{-1}

DKDT_GEN	Generation of kinetic energy	W m^{-2}
TEFIXER	Total energy added by artificial energy "fixer"	W m^{-2}

A tendency may be expressed as the sum of dynamics, physics, and analysis variables. For example, the tendency of vertically integrated water vapor (precipitable water) is expressed using MERRA variables as follows.

$$\frac{\partial W_{(v)}}{\partial t} := DQVDT\_DYN + DQVDT\_PHY + DQVDT\_ANA \tag{5}$$

Equation (2) is represented as follows.

$$\begin{aligned}\frac{\partial A_E}{\partial t} := {} & L_v \cdot (DQVDT\_DYN + DQVDT\_PHY + DQVDT\_ANA) \\ & - L_f \cdot (DQIDT\_DYN + DQIDT\_PHY + DQIDT\_ANA) \\ & + DHDT\_DYN + DHDT\_PHY + DHDT\_ANA \\ & + DPDT\_DYN + DPDT\_PHY + DPDT\_ANA \\ & + DKDT\_DYN + DKDT\_PHY + DKDT\_ANA\end{aligned} \tag{6}$$

Equation (3) is represented as:

$$\begin{aligned}\nabla \cdot \tilde{\mathbf{F}}_A := {} & -(L_v \cdot DQVDT\_DYN - L_f \cdot DQIDT\_DYN \\ & + CONVKE + CONVCPT + CONVPHI)\end{aligned} \tag{7}$$

Equations (4) and (5) are represented as follows.

$$\begin{aligned}R_{top} + F_{sfc} := {} & (SWTNT - LWTUP) - (SWGNT + LWGNT) \\ & + EFLUX + HFLUX + L_f \cdot PRECSN\end{aligned} \tag{8}$$

The contribution of spurious residuals in the energy term is represented as:

$$\begin{aligned}Q_{NUM} := {} & -DKDT\_DYN + CONVKE + CONVPHI \\ & + DKDT\_GEN - DPDT\_DYN - TEFIXER\end{aligned} \tag{9}$$

The remainder of equation (1) is given as follows.

$$\begin{aligned}L_v \left.\frac{\partial W_v}{\partial t}\right|_{CHM} + \left[L_v \frac{\partial W_v}{\partial t} - L_f \frac{\partial W_i}{\partial t}\right]_{FIL} + ANA_{(E)} := {} & \\ L_v \cdot DQVDT\_CHM + (L_v \cdot DQVDT\_FIL - L_f \cdot DQIDT\_FIL) & \\ + (L_v \cdot DQVDT\_ANA - L_f \cdot DQIDT\_ANA + DHDT\_ANA & \\ + DKDT\_ANA + DPDT\_ANA) &\end{aligned} \tag{10}$$

684 REFERENCES

685 Barkstrom, B.R., 1984: The Earth Radiation Budget Experiment (ERBE). *Bull. Amer. Meteor.*
686 *Soc.*, **65**, 1170-1185.
687 Bloom, S., L. Takacs, A. DaSilva, and D. Ledvina, 1996: Data assimilation using incremental
688 analysis updates. *Mon. Wea. Rev.*, **124**, 1256-1271.
689 Bosilovich, M.G., F.R. Robertson, and J. Chen, 2010: Global energy and water budgets in
690 MERRA. *J. Climate* (in review).
691 Bretherton, C.S., S.R. de Roode, C. Jakob, E.L. Andreas, J. Intrieri, and R.E. Moritz, and P.O.G.
692 Persson, 2000: A comparison of the ECMWF forecast model with observations over the
693 annual cycle at SHEBA. Unpublished manuscript, 46 pp. (Available from
694 http://citeseerx.ist.psu.edu/viewdoc/download?doi=10.1.1.36.9608&rep=rep1&type=pdf).
695 Briegleb, B.P, and D.H. Bromwich, 1998: Polar climate simulations of the NCAR CCM3. *J.*
696 *Climate*, 11, 1270-1286.
697 Carroll, J.J., 1982: Long-term means and short-term variability of the surface energy balance
698 components at South Pole. *J. Geophys. Res.*, **87**, 4277-4286.
699 Comiso, J.C., 2000: Variability and trends in Antarctic surface temperatures from in situ and
700 satellite infrared measurements. *J. Climate*, **13**, 1674-1696.
701 Compo, G.P., J.S. Whitaker, and P.D. Sardeshmukh, 2006: Feasibility of a 100-year reanalysis
702 using only surface pressure data. *Bull. Amer. Meteor. Soc.*, **87**, 175-190.
703 Cullather, R.I., and M.G. Bosilovich, 2010: The moisture budget of the polar atmosphere in
704 MERRA. *J. Climate*, submitted.
705 Curry, J.A., J.L. Schramm, D.K. Perovich, and J.O. Pinto, 2001: Applications of SHEBA/FIRE
706 data to evaluation of snow/ice albedo parameterizations. *J. Geophys. Res.*, **106**, 15,345–
707 15,355.
708 Duynkerke, P., and S. de Roode, 2001: Surface energy balance and turbulence characteristics
709 observed at the SHEBA Ice Camp during FIRE III. *J. Geophys. Res.*, **106**, 15313-15322.
710 Dutton, E.G., R.S. Stone, J.J. DeLuisi, 1989: South Pole surface radiation balance measurements,
711 April 1986 to February 1988. *NOAA ERL Air Resources Laboratory Data Report Series*, **17**,
712 49 pp.
713 Fasullo, J.T., and K.E. Trenberth, 2008: The annual cycle of the energy budget. Part I. Global
714 mean and land–ocean exchanges. *J. Climate*, **21**, 2297-2312.
715 Genthon, C., and G. Krinner, 1998: Convergence and disposal of energy and moisture on the
716 Antarctic polar cap from ECMWF Reanalyses and Forecasts. *J. Climate*, **11**, 1703-1716.
717 Gibson, J.K., P. Kållberg, S. Uppala, A. Hernandez, A. Nomura, and E. Serrano, 1997: *ERA*
718 *Description*. ECMWF Reanalyis Project Report Series, No. 1, 72 pp.
719 Josey, S.A., 2009: Southern Ocean air-sea flux climatologies and uncertainties.
720 CLIVAR/CliC/SCAR Southern Ocean Region Implementation Panel 5th Meeting, 16-18
721 February 2009, Sydney, Australia (PowerPoint presentation) [Available from Climate
722 Variability & Predictability project (CLIVAR), World Climate Research Programme,
723 http://www.clivar.org/organization/southern/sop5_talks.php].

724 Kalnay, E., M. Kanamitsu, R. Kistler, W. Collins, D. Deaven, L. Gandin, M. Iredell, S. Saha, G.
725 White, J. Woollen, Y. Zhu, A. Leetmaa, R. Reynolds, M. Chelliah, W. Ebisuzaki, W.Higgins,
726 J. Janowiak, K. C. Mo, C. Ropelewski, J. Wang, R. Jenne, and D. Joseph, 1996: The
727 NCEP/NCAR 40-Year Reanalysis Project. *Bull. Amer. Meteorol. Soc.*, **77**, 437-472.
728 King, J.C., and J. Turner, 1997: *Antarctic Meteorology and Climatology*. Cambridge Univ. Press,
729 United Kingdom, 409 pp.
730 Levitus, S., 1984: Annual cycle of temperature and heat storage in the world ocean. *J. Phys.*
731 *Ocean.*, **14**, 727-746.
732 Lin, B., P. Minnis, A. Fan, J.A. Curry, and H. Gerber, 2001: Comparison of cloud liquid water
733 paths derived from in situ and microwave radiometer data taken during the
734 SHEBA/FIREACE. *Geophys. Res. Lett.*, **28**, 975-978.
735 Moore, J.K., M.R. Abbott, and J.G. Richman, 1999: Location and dynamics of the Antarctic
736 Polar Front from satellite sea surface temperature data. *J. Geophys. Res.*, **104**, 3059–3073.
737 Nakamura, N., and A.H. Oort, 1988: Atmospheric heat budgets of the polar regions. *J. Geophys.*
738 *Res.*, **93**, 9510-9524.
739 Ohata, T., N. Ishikawa, S. Kobayashi, and S. Kawaguchi, 1985: Heat balance at the snow surface
740 in a katabatic wind zone, East Antarctica. *Ann. Glaciol.*, **6**, 174-177.
741 Okada, I., and T. Yamanouchi, 2002: Seasonal change of the atmospheric heat budget over the
742 Southern Ocean from ECMWF and ERBE data. *J. Climate*, **15**, 2527-2536.
743 Onogi, K., J. Tsutsui, H. Koide, M. Sakamoto, S. Kobayashi, H. Hatsushika, T. Matsumoto, N.
744 Yamazaki, H. Kamahori, K. Takahashi, S. Kadokura, K. Wada, K. Kato, R. Oyama, T. Ose,
745 N. Mannoji, and R. Taira, 2007: The JRA-25 reanalysis. *J. Meteor. Soc. Japan*, **85**, 369–432.
746 Oort, A.H., 1983: Global atmospheric circulation statistics, 1958-1973. *NOAA Professional*
747 *Paper No. 14*, U.S. Government Printing Office, Washington, DC, 180 pp.+47 microfiches.
748 Porter, D.F., J.J. Cassano, M.C. Serreze, and D.N. Kindig, 2010: New estimates of the large-
749 scale Arctic atmosphere energy budget. *J. Geophys. Res.*, **115**, D08108,
750 doi:10.1029/2009JD012653.
751 Randall, D., J. Curry, D. Battisti, G. Flato, R. Grumbine, S. Hakkinen, D. Martinson, R. Preller,
752 J. Walsh, and J. Weatherly, 1998: Status of and outlook for large-scale modeling of
753 atmosphere–ice–ocean interactions in the Arctic. *Bull. Amer. Meteor. Soc.*, **79**, 197-219.
754 Reijmer, C.H., and J. Oerlemans, 2002: Temporal and spatial variability of the surface energy
755 balance in Dronning Maud Land, East Antarctica. *J. Geophys. Res.*, **107**, 4759,
756 doi:10.1029/2000JD000110.
757 Rienecker, M.M., M.J. Suarez, R. Todling, J. Bacmeister, L. Takacs, H.-C. Liu, W. Gu, M.
758 Sienkiewicz, R.D. Koster, R. Gelaro, I. Stajner, and E. Nielsen, 2009: *The GEOS-5 Data*
759 *Assimilation System- Documentation of Versions 5.0.1, 5.1.0, and 5.2.0*. Technical Report
760 Series on Global Modeling and Data Assimilation, NASA/TM-2007-104606, M.J. Suarez,
761 Ed., Vol. 27, 95 pp.
762 Rienecker, M.M., and coauthors, 2010: The NASA Modern Era Retrospective-Analysis for
763 Research and Applications (MERRA). *J. Climate* (in preparation).

764 Saha, S., S. Moorthi, H.-L. Pan, X. Wu, J. Wang, S. Nadiga, P. Tripp, R. Kistler, J. Woollen, D.
765 Behringer, H. Liu, D. Stokes, R. Grumbine, G. Gayno, J. Wang, Y.-T. Hou, H. Chuang, H.H.
766 Juang, J. Sela, M. Iredell, R. Treadon, D. Kleist, P. Van Delst, D. Keyser, J. Derber, M. Ek, J.
767 Meng, H. Wei, R. Yang, S. Lord, H. van den Dool, A. Kumar, W. Wang, C. Long, M.
768 Chelliah, Y. Xue, B. Huang, J.-K. Schemm, W. Ebisuzaki, R. Lin, P. Xie, M. Chen, S. Zhou,
769 W. Higgins, C.-Z. Zou, Q. Liu, Y. Chen, Y. Han, L. Cucurull, R.W. Reynolds, G. Rutledge,
770 and M. Goldberg, 2010: The NCEP Climate Forecast System Reanalysis. *Bull. Amer. Meteor.*
771 *Soc.*, submitted.
772 Serreze, M.C., A.P. Barrett, A.G. Slater, M. Steele, J. Zhang, and K.E. Trenberth, 2007:
773 The large-scale energy budget of the Arctic. *J. Geophys. Res.*, **112**, D11122,
774 doi:10.1029/2006JD008230.
775 Simmons, A.J., S. Uppala, D. Dee, and S. Kobayashi, 2007: ERA-Interim: New ECMWF
776 reanalysis products from 1989 onwards. *ECMWF Newsletter*, **110**, 25–35.
777 Thorne, P.W., and R.S. Vose, 2010: Reanalyses suitable for characterizing long-term trends. Are
778 they really achievable? *Bull. Amer. Meteor. Soc.*, **91**, 353-361.
779 Trenberth, K.E., 1997: Using atmospheric budgets as a constraint on surface fluxes. *J. Climate*,
780 **10**, 2796-2809.
781 Uppala, S.M., P.W. Kållberg, A.J. Simmons, U. Andrae, V. da Costa Bechtold, M. Fiorino, J.K.
782 Gibson, J. Haseler, A. Hernandez, G.A. Kelly, X. Li, K. Onogi, S. Saarinen, N. Sokka, R.P.
783 Allan, E. Andersson, K. Arpe, M.A. Balmaseda, A.C.M. Beljaars, L. van de Berg, J. Bidlot,
784 N. Bormann, S. Caires, F. Chevallier, A. Dethof, M. Dragosavac, M. Fisher, M. Fuentes, S.
785 Hagemann, E. Hólm, B.J. Hoskins, L. Isaksen, P.A.E.M. Janssen, R. Jenne, A.P. McNally, J.-
786 F. Mahfouf, J.-J. Morcrette, N.A. Rayner, R.W. Saunders, P. Simon, A. Sterl, K.E. Trenberth,
787 A. Untch, D. Vasiljevic, P. Viterbo, and J. Woollen, 2005: The ERA-40 re-analysis. *Quart. J.*
788 *R. Meteorol. Soc.*, **131**, 2961-3012.
789 Uttal, T., J.A. Curry, M.G. Mcphee, D.K. Perovich, R.E. Moritz, J.A. Maslanik, P.S. Guest, H.L.
790 Stern, J.A. Moore, R. Turenne, A. Heiberg, M.C. Serreze, D.P. Wylie, O.G. Persson, C.A.
791 Paulson, C. Halle, J.H. Morison, P.A. Wheeler, A. Makshtas, H. Welch, M.D. Shupe, J.M.
792 Intrieri, K. Stamnes, R.W. Lindsey, R. Pinkel, W.S. Pegau, T.P. Stanton, and T.C. Grenfeld,
793 2002: Surface Heat Budget of the Arctic Ocean. *Bull. Amer. Meteor. Soc.*, **83**, 255–275.
794 Wielicki, B.A., B.R. Barkstrom, E.F. Harrison, R.B. Lee, G.L. Smith, and J.E. Cooper, 1996:
795 Clouds and the Earth's Radiant Energy System (CERES): An Earth Observing System
796 experiment. *Bull. Amer. Meteor. Soc.*, **77**, 853-868.
797
798

List of Table Captions

TABLE 1. Components of the MERRA atmospheric energy budget for regions defined in Fig. 1, in W m^{-2}. The surface flux F_{sfc} discounts latent heating from solid precipitation. The standard deviation over the 1979-2005 time period is indicated in parentheses.

TABLE 2. MERRA, CFSR, and ERA-I 1989-2005 average TOA and surface energy flux values for regions defined in Fig. 1, in W m^{-2}. The standard deviation over the time period is indicated in parentheses.

List of Figure Captions

FIGURE 1. Regions of study for (a.) the Northern Hemisphere and (b.) the Southern Hemisphere. Bold line indicates the 70° parallel. Continental areas are shaded gray.

FIGURE 2. Average MERRA analysis increments field for the atmospheric energy budget (variable $ANA_{(E)}$) for (a.) the Northern Hemisphere and (b.) the Southern Hemisphere. The contour interval is 20 W m^{-2}. The zero contour is indicated with a solid black line.

FIGURE 3. Annual cycle of atmospheric energy budget components in MERRA for (a.) north polar cap, (b.) south polar cap, and (c.) the Southern Ocean domain, in W m^{-2}. Bars indicate plus and minus the standard deviation for the period 1979-2005.

FIGURE 4. Average monthly meridional energy transport from MERRA (a.) across 70°N, contoured every $5 \cdot 10^9$ W m^{-1}, and (b.) 70°S, contoured every $3 \cdot 10^9$ W m^{-1}. Positive values indicate northward transport.

FIGURE 5. Annual average net surface heat flux from MERRA (positive upwards). Contours are plotted with an interval of 20 W m^{-2} and for the levels −10, −5, 0, 5, and 10 W m^{-2}. The zero contour is indicated with a solid black line.

FIGURE 6. Monthly averaged surface albedo (gray) and upwelling shortwave radiative flux (dark) for SHEBA observed (solid) and corresponding MERRA values (dashed) for October 1997 to September 1998, in W m^{-2}. "Tower" values are from downward-pointing pyranometer measurements, while "line albedo" values are from surface measurements along a 300m line.

FIGURE 7. Near-surface hourly air temperature from SHEBA and corresponding values from MERRA for the period 1 February 1998 to 30 June 1998, in degrees C.

FIGURE 8. Time series of monthly averaged near-surface station air temperature anomaly and corresponding MERRA values for Barrow (left, 71°N, 157°W) and Jan Mayen (right, 71°N, 9°W), in degrees C.

FIGURE 9. Hourly (a.) precipitable water and (b.) liquid water path from SHEBA microwave radiometer and corresponding MERRA values, in mm.

843 FIGURE 10. Average annual time series for near surface station temperature and corresponding
844 MERRA values for (a.) Amundsen-Scott (90°S), and (b.) Scott Base (78°S, 167°E), in degrees C.
845 Bars indicate the standard deviation of monthly values over the period 1979–2005.
846
847 FIGURE 11. Time series of daily downwelling longwave flux and the net downward flux from
848 Dutton et al. (1989) and corresponding values from MERRA for 90°S, in W m^{-2}.
849

TABLE 1. Components of the MERRA atmospheric energy budget for regions defined in Fig. 1, in W m^{-2}. The surface flux F_{sfc} discounts latent heating from solid precipitation. The standard deviation over the 1979-2005 time period is indicated in parentheses.

		$\partial E/\partial t$	$-\nabla \cdot F_A$	R_{top}	F_{sfc}	$ANA_{(E)}$	Q_{NUM}
70°N – 90°N	January	−1(11)	110(16)	−173(4)	63(5)		−5(9)
	July	2(6)	81(8)	2(3)	−68(4)		−13(5)
	Mean	0(2)	99(4)	−110(1)	19(1)		−11(5)
Arctic Ocean	January	−3(13)	106(19)	−176(4)	70(5)		−5(14)
	July	3(9)	96(10)	−7(4)	−75(6)		−9(6)
	Mean	0(2)	99(6)	−114(1)	23(2)		−9(7)
Greenland	January	−2(19)	143(26)	−153(6)	−1(4)		4(16)
	July	1(8)	118(19)	−48(1)	−40(1)		−32(16)
	Mean	0(2)	138(9)	−112(1)	−16(1)		−14(9)
70°S – 90°S	January	−1(10)	78(10)	−25(2)	−32(2)		−23(8)
	July	−10(13)	131(16)	−142(3)	19(2)		−21(10)
	Mean	0(1)	118(6)	−101(1)	3(1)		−22(6)
Southern Ocean	January	2(6)	97(17)	58(10)	−114(9)		−40(17)
	July	−7(8)	91(15)	−174(1)	82(3)		−11(13)
	Mean	0(1)	89(5)	−83(2)	12(2)		−23(5)
Antarctica	January	−2(10)	80(11)	−41(1)	−21(1)		−21(8)
	July	−9(12)	135(18)	−134(3)	7(2)		−20(10)
	Mean	0(1)	124(5)	−101(1)	−3(1)		−23(5)

TABLE 2. MERRA, CFSR, and ERA-I 1989-2005 average TOA and surface energy flux values for regions defined in Fig. 1, in W m^{-2}. The standard deviation over the time period is indicated in parentheses.

		R_{top}			F_{sfc}		
		MERRA	CFSR	ERA-I	MERRA	CFSR	ERA-I
70°N – 90°N	January	−172(4)	−172(5)	−174(4)	64(6)	55(7)	59(7)
	July	2(3)	−1(3)	0(3)	−69(4)	−87(5)	−78(4)
	Mean	−110(2)	−114(1)	−114(1)	19(1)	14(1)	12(2)
Arctic Ocean	January	−176(4)	−174(5)	−177(4)	70(5)	59(7)	55(5)
	July	−5(4)	−2(3)	−1(3)	−79(6)	−106(8)	−90(6)
	Mean	−114(1)	−115(1)	−117(1)	23(1)	12(2)	12(2)
Greenland	January	−152(5)	−159(5)	−159(5)	0(3)	6(1)	11(2)
	July	−48(1)	−58(2)	−51(2)	−40(1)	−12(2)	−15(1)
	Mean	−112(1)	−120(2)	−116(2)	−16(1)	1(0)	2(0)
70°S – 90°S	January	−26(2)	−34(3)	−20(2)	−31(2)	−19(2)	−22(2)
	July	−142(2)	−147(3)	−146(3)	19(2)	16(4)	12(2)
	Mean	−101(1)	−109(1)	−102(1)	3(1)	7(2)	3(1)
Southern	January	55(11)	76(5)	72(3)	−111(9)	−145(5)	−133(3)
Ocean	July	−173(1)	−172(1)	−177(1)	81(10)	84(5)	67(3)
	Mean	−84(3)	−77(2)	−84(1)	13(2)	3(5)	−1(1)
Antarctica	January	−41(1)	−54(2)	−38(2)	−21(1)	−2(0)	−5(1)
	July	−134(3)	−140(3)	−138(3)	7(2)	2(0)	3(1)
	Mean	−101(1)	−109(1)	−100(1)	−3(1)	1(0)	0(0)

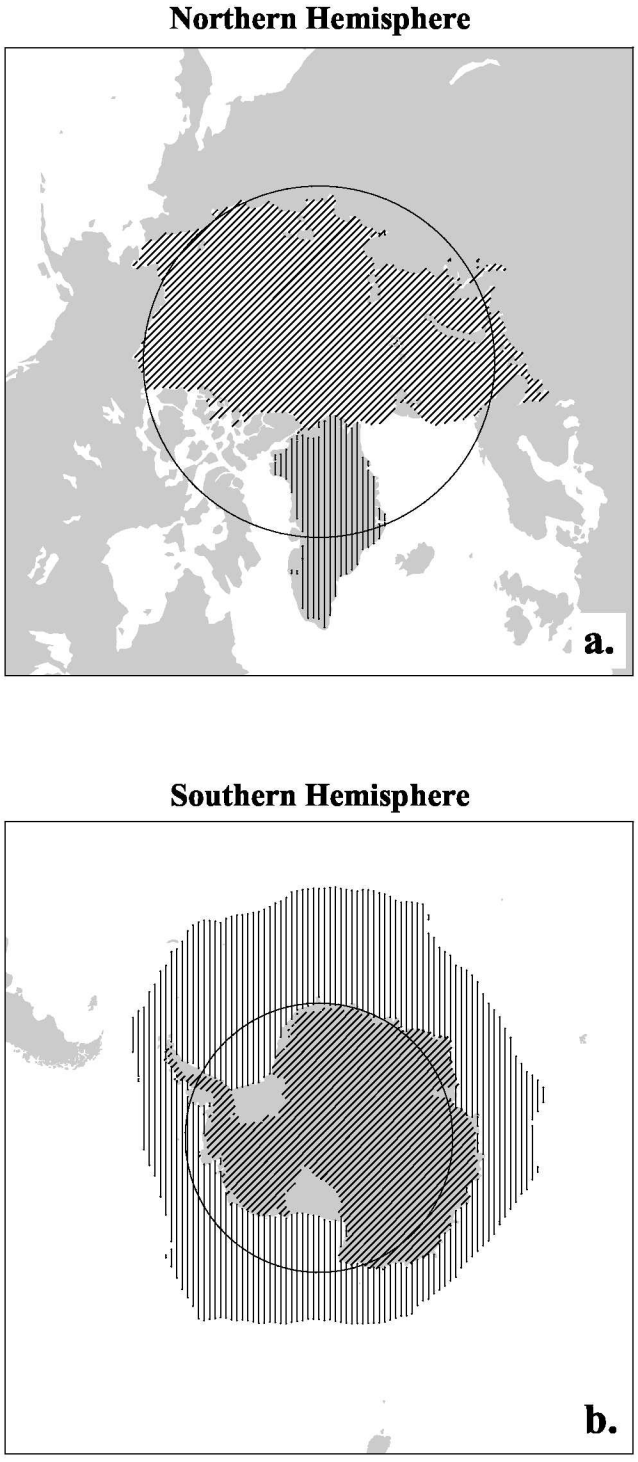

FIGURE 1. Regions of study for (a.) the Northern Hemisphere and (b.) the Southern Hemisphere. Bold line indicates the 70° parallel. Continental areas are shaded gray.

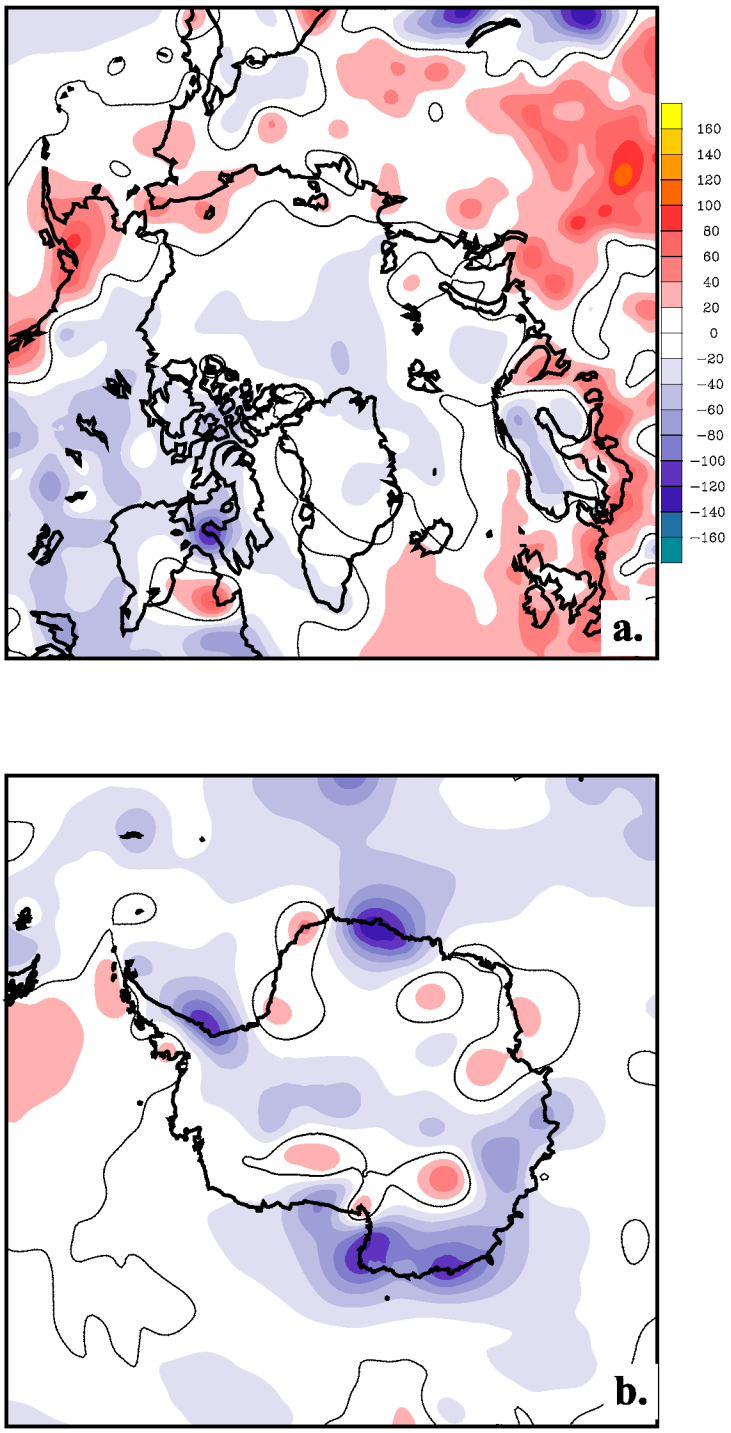

FIGURE 2. Average MERRA analysis increments field for the atmospheric energy budget (variable $ANA_{(E)}$) for (a.) the Northern Hemisphere and (b.) the Southern Hemisphere. The contour interval is 20 W m^{-2}. The zero contour is indicated with a solid black line.

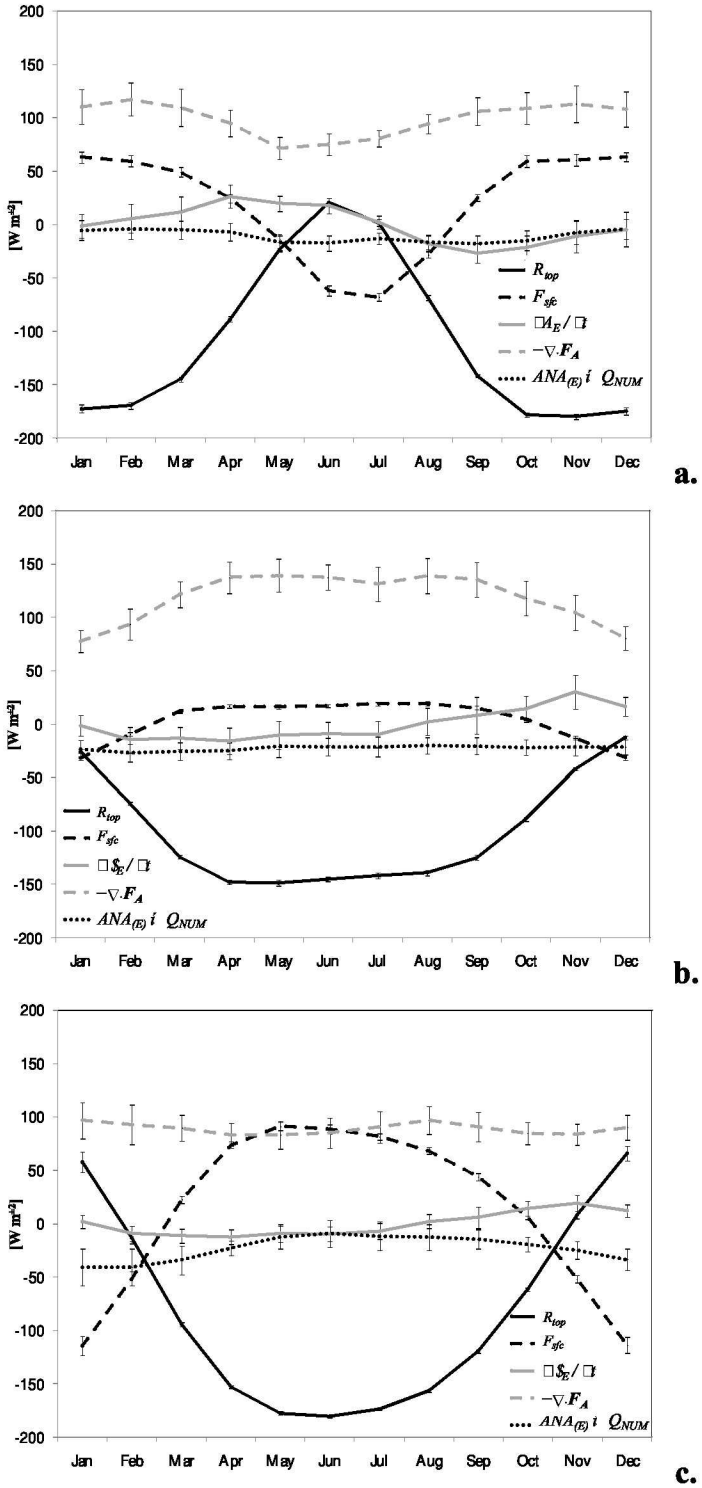

FIGURE 3. Annual cycle of atmospheric energy budget components in MERRA for (a.) north polar cap, (b.) south polar cap, and (c.) the Southern Ocean domain, in W m^{-2}. Bars indicate plus and minus the standard deviation for the period 1979-2005.

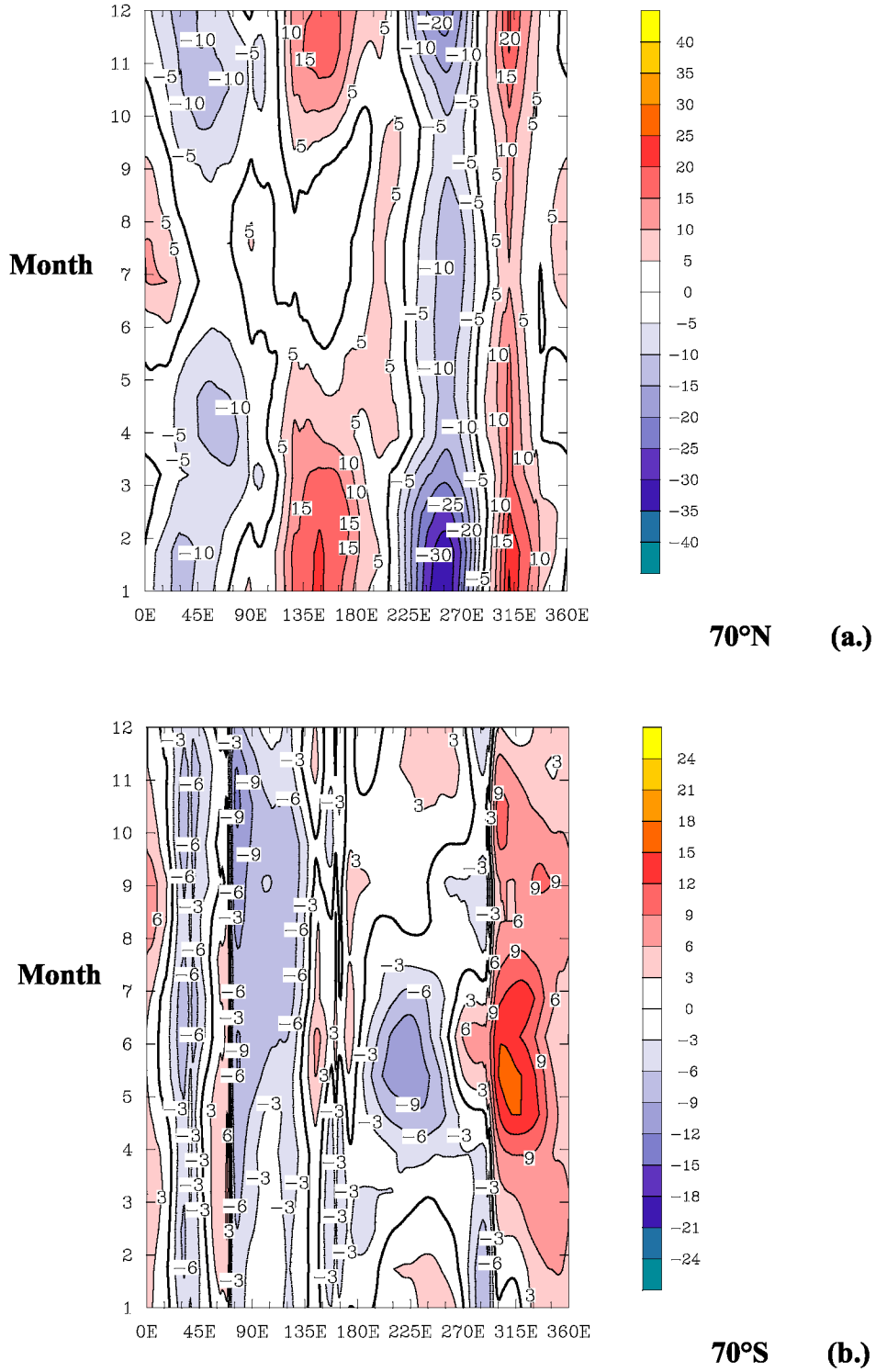

FIGURE 4. Average monthly meridional energy transport from MERRA (a.) across 70°N, contoured every $5 \cdot 10^9$ W m^{-1}, and (b.) 70°S, contoured every $3 \cdot 10^9$ W m^{-1}. Positive values indicate northward transport.

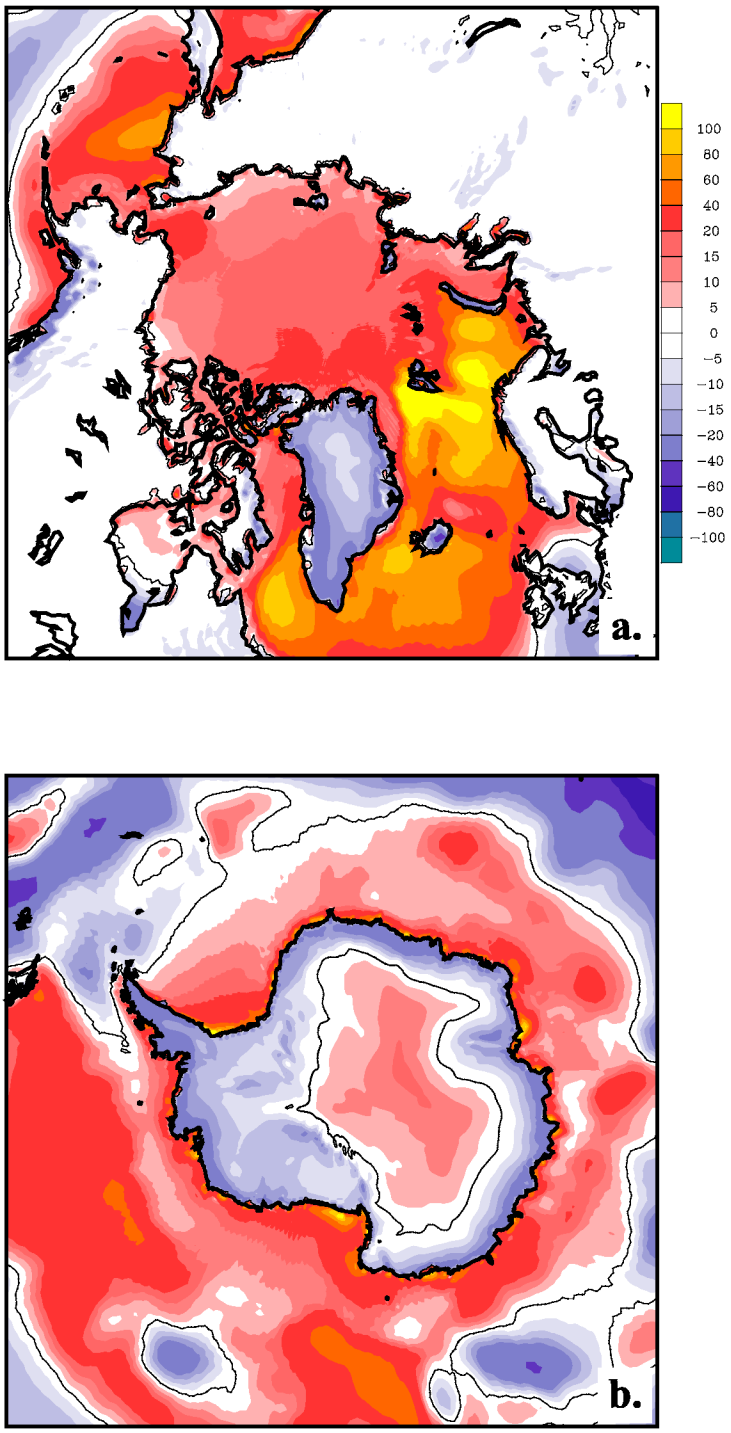

FIGURE 5. Annual average net surface heat flux from MERRA (positive upwards). Contours are plotted with an interval of 20 W m^{-2} and for the levels −10, −5, 0, 5, and 10 W m^{-2}. The zero contour is indicated with a solid black line.

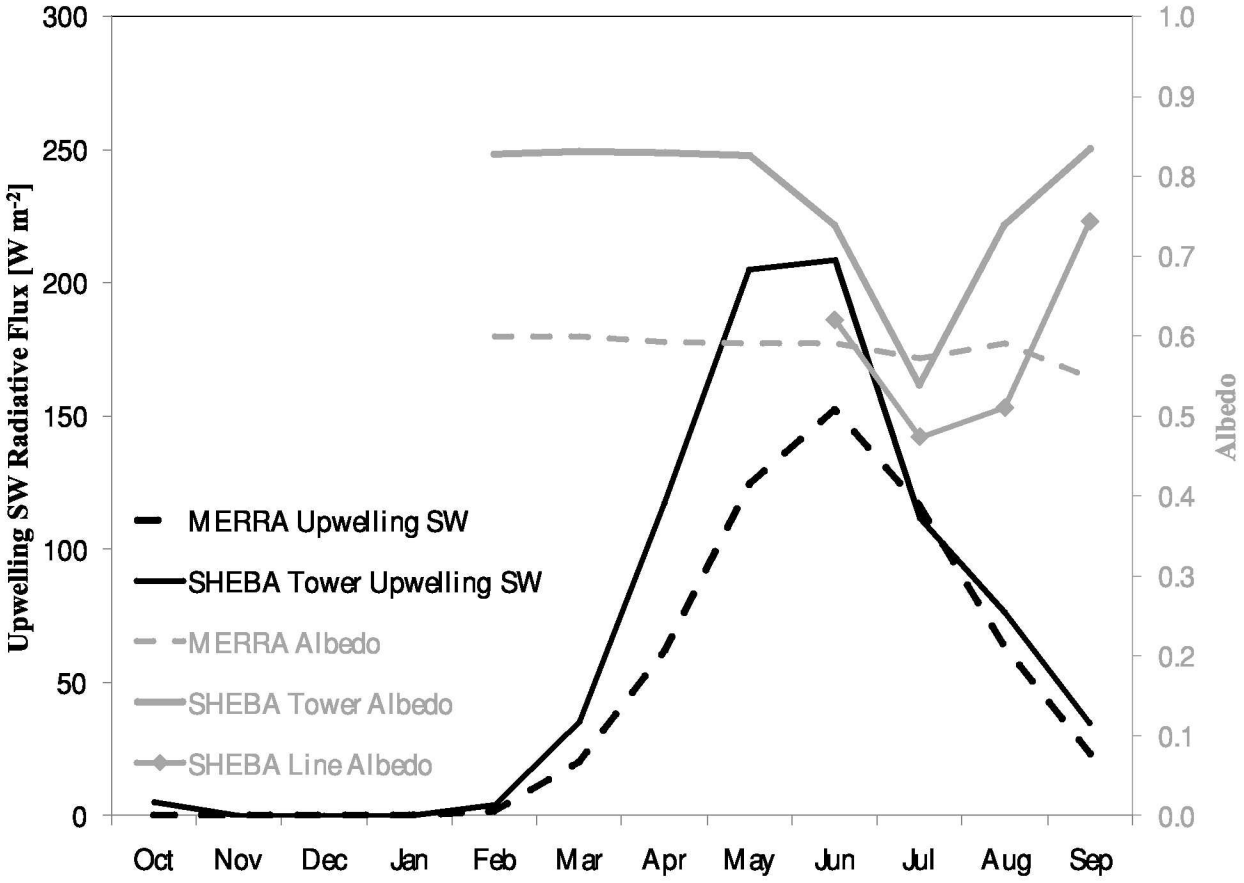

FIGURE 6. Monthly averaged surface albedo (gray) and upwelling shortwave radiative flux (dark) for SHEBA observed (solid) and corresponding MERRA values (dashed) for October 1997 to September 1998, in W m^{-2}. "Tower" values are from downward-pointing pyranometer measurements, while "line albedo" values are from surface measurements along a 300m line.

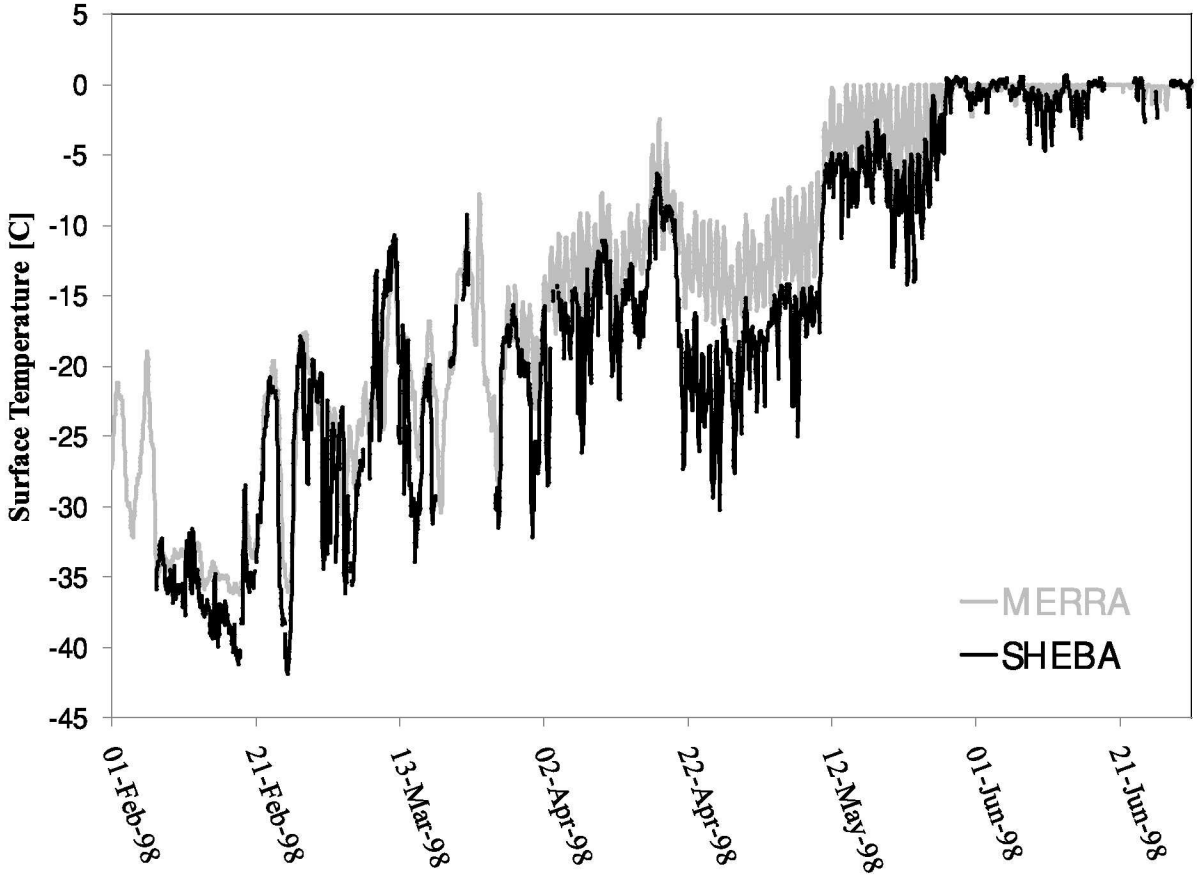

FIGURE 7. Near-surface hourly air temperature from SHEBA and corresponding values from MERRA for the period 1 February 1998 to 30 June 1998, in degrees C.

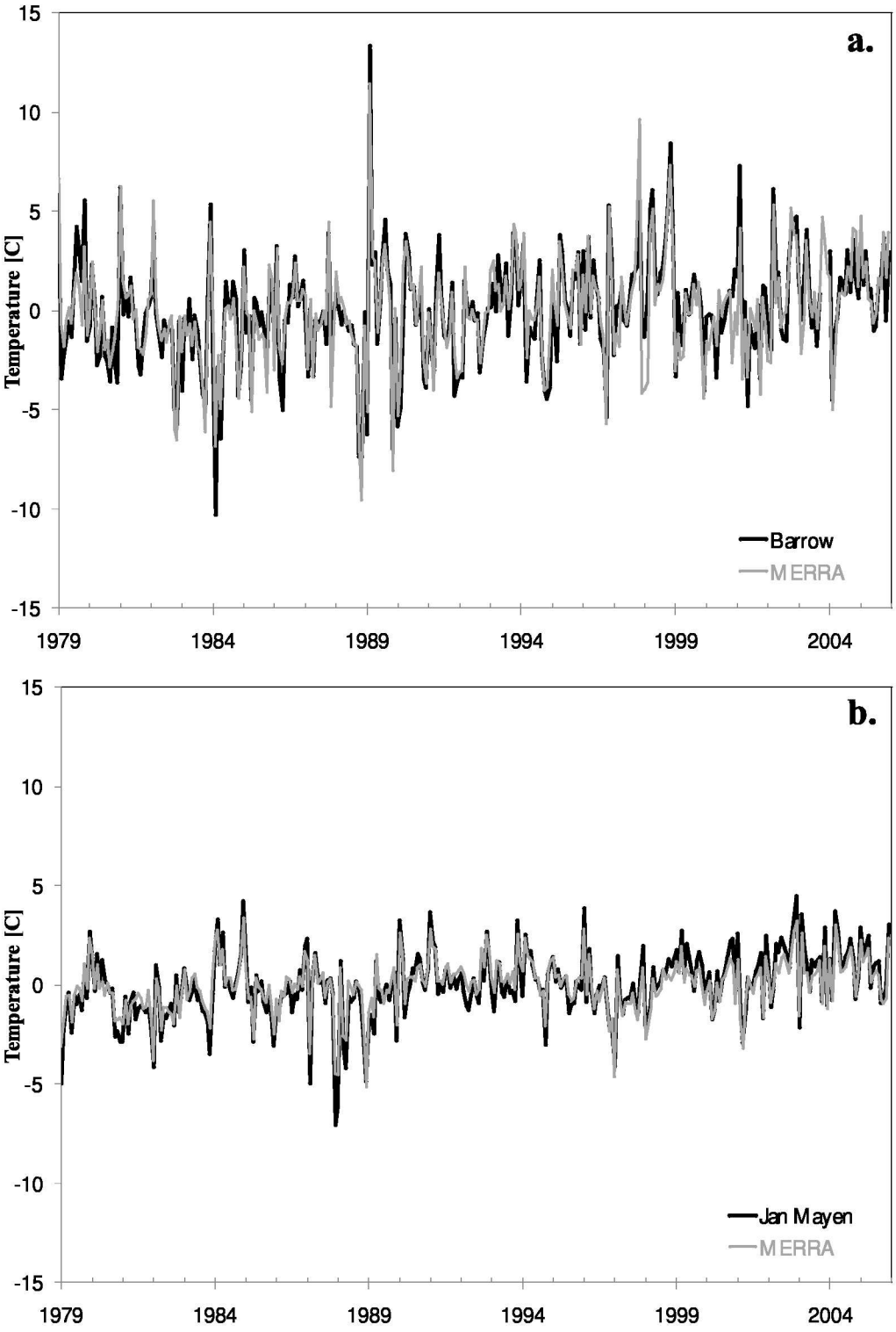

FIGURE 8. Time series of monthly averaged near-surface station air temperature anomaly and corresponding MERRA values for Barrow (left, 71°N, 157°W) and Jan Mayen (right, 71°N, 9°W), in degrees C.

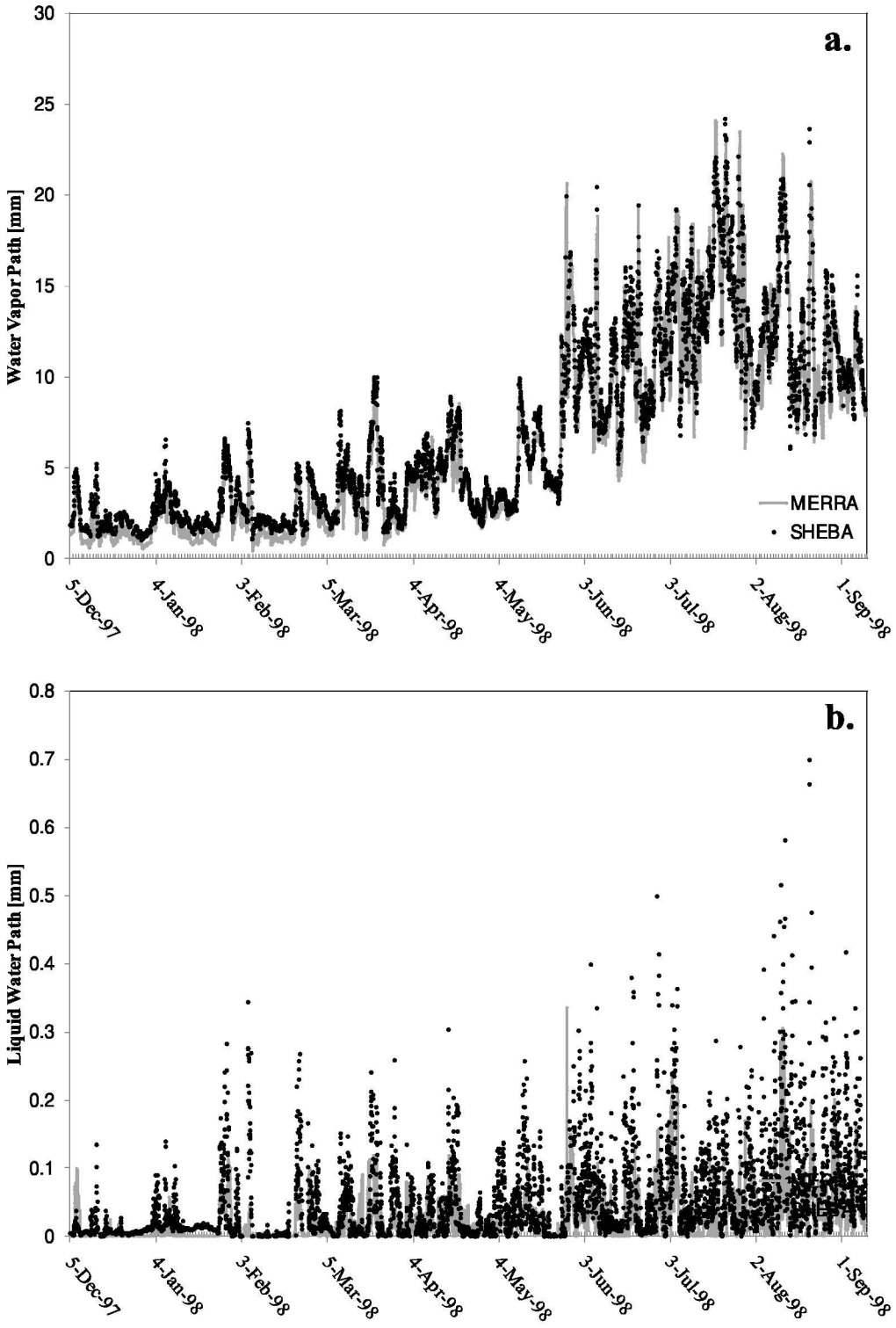

FIGURE 9. Hourly (a.) precipitable water and (b.) liquid water path from SHEBA microwave radiometer and corresponding MERRA values, in mm.

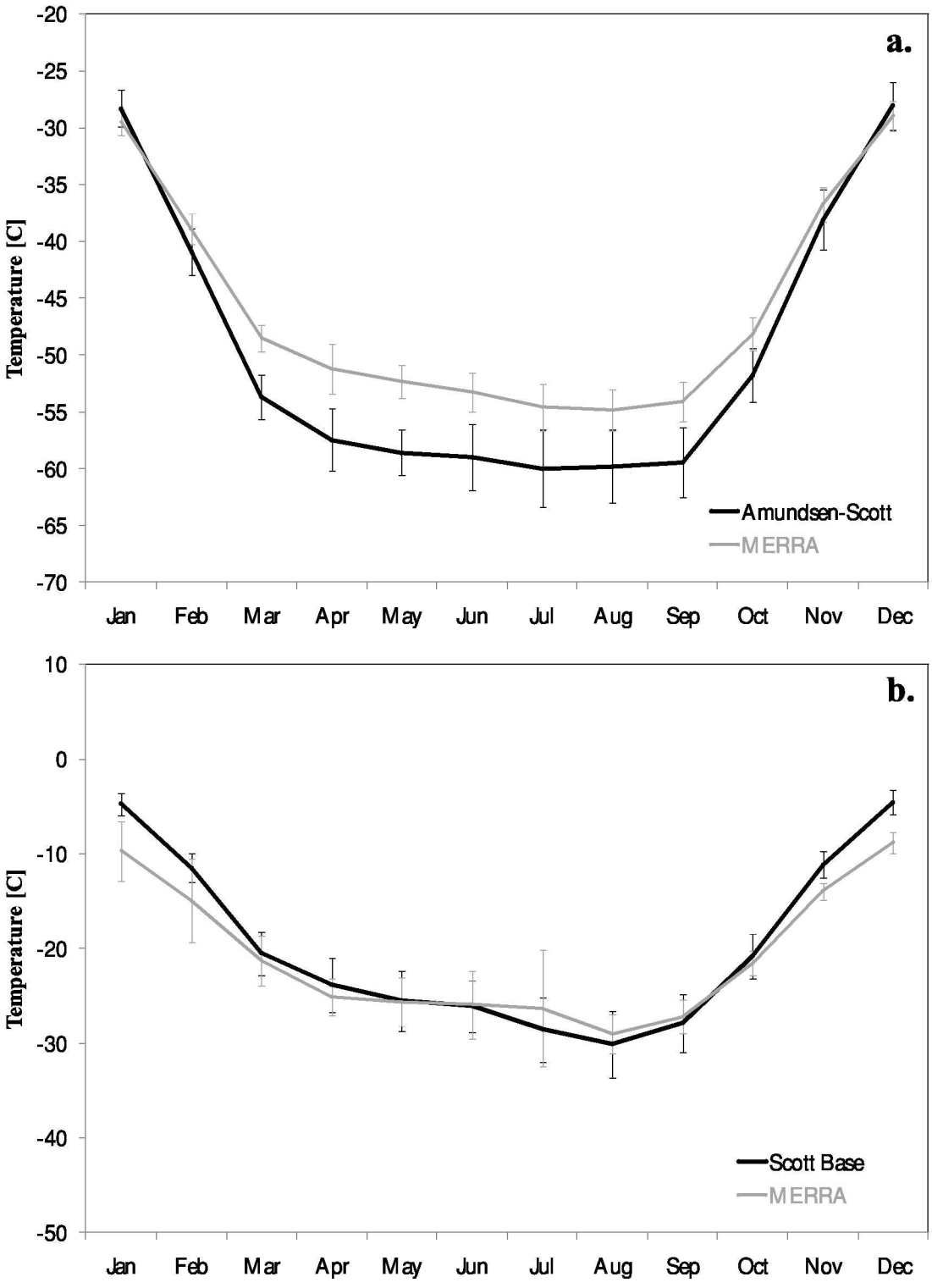

FIGURE 10. Average annual time series for near surface station temperature and corresponding MERRA values for (a.) Amundsen-Scott (90°S), and (b.) Scott Base (78°S, 167°E), in degrees C. Bars indicate the standard deviation of monthly values over the period 1979–2005.

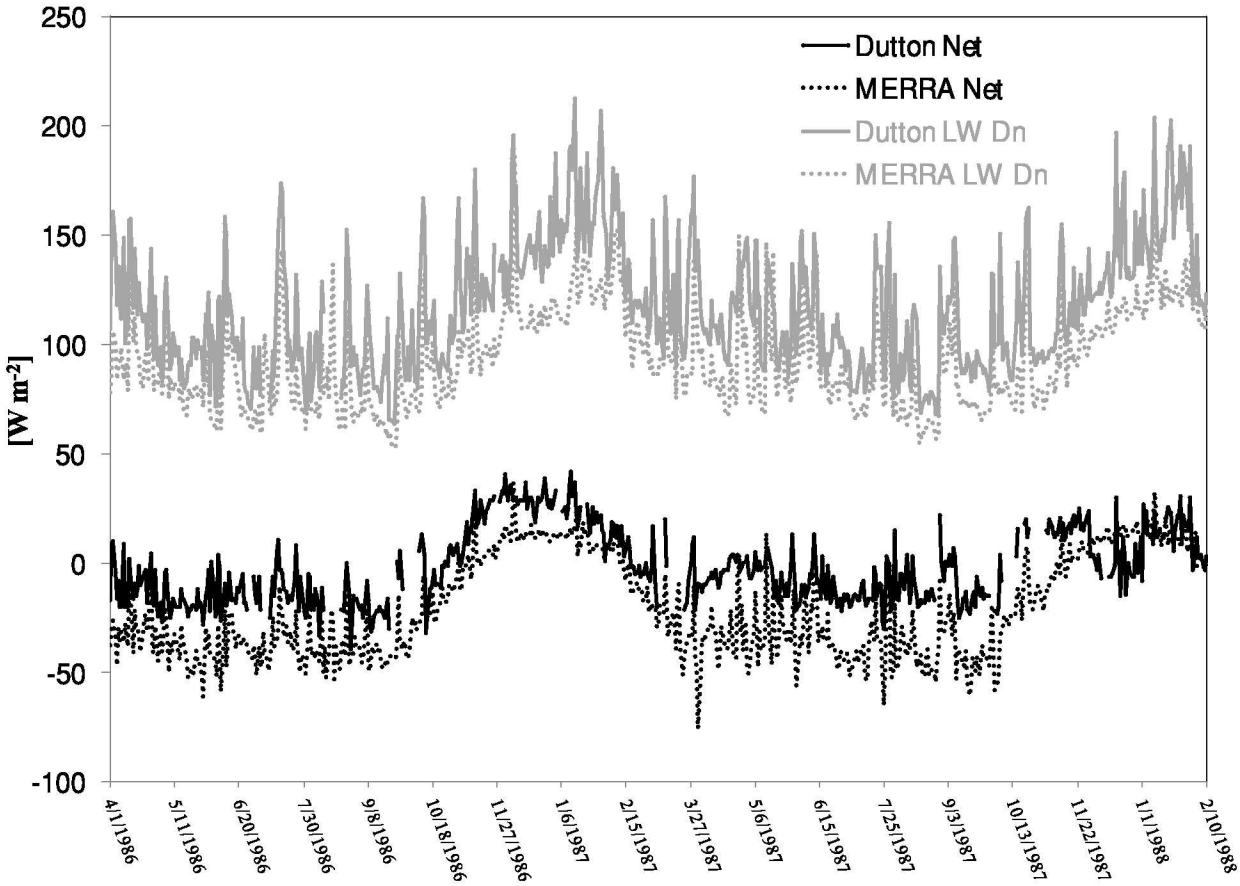

FIGURE 11. Time series of daily downwelling longwave flux and the net downward flux from Dutton et al. (1989) and corresponding values from MERRA for 90°S, in W m^{-2}.